Accepted Manuscript

The influence of deformation limits on fluid-structure interactions in underwater blasts

Y. Yuan, P.J. Tan, K.A. Shojaei, P. Wrobel

Please cite this article as: Y. Yuan, P.J. Tan, K.A. Shojaei, P. Wrobel, The influence of deformation limits on fluid-structure interactions in underwater blasts, *International Journal of Impact Engineering* (2016), doi: 10.1016/j.ijimpeng.2016.11.007

Highlights

- The classical FSI problem is revisited for a fully clamped elastoplastic beam
- Beneficial effects of FSI depends on the transverse deflection and time to detachment
- Impulse transmitted is reduced by increasing aspect ratio in mode I deformation
- Decreasing aspect ratio always reduces impulse transmitted in modes II and III

The influence of deformation limits on fluid-structure interactions in underwater blasts

Y. Yuan[†], P. J. Tan[*], K. A. Shojaei, P. Wrobel

Department of Mechanical Engineering, University College London, Torrington Place, London WC1E 7JE, UK

Abstract

This paper revisits a classical fluid-structure interaction (FSI) problem on the momentum and energy transfer to a structure from an underwater blast. Hitherto, the majority of analytical models assume a rigid (non-deformable) and free-standing (unsupported) structure where resistance to its translational motion - apart from that offered by its inertial mass - comes from 'ad-hoc' backing spring(s) introduced to simulate compression of the fluid medium and/or the resistance to transverse deformation encountered by a real structure. These limitations/assumptions are relaxed in this paper by adopting a physically realistic fully-clamped ductile beam system that takes into account large elasto-plastic deformation, limits to material deformation, boundary compliance and boundary failure; the analytical framework was developed previously by Yuan et al. [1]. By coupling the fluid (water) domain to the analytical model of the ductile beam system, the momentum and energy transferred by the blast wave are critically re-evaluated for non-impulsive loading régime; in particular, on how the beam's deformation mode and boundary compliance affects fluid and structure interaction, up until the point of complete beam detachment from its supports. Detailed finite-element models were also developed to simulate the interactions between the fluid and structural beam where predictions were in good agreement with those by the analytical model. Sensitivity analyses were carried out that offer new insights on the influence of the beam's aspect ratio and inertial mass.

Keywords: Fluid-structure interaction, Underwater blast, Limits to deformation, Energy and momentum transfer, Ductile damage

[†]Currently at Department of Automotive Engineering, Tsinghua University, Beijing, China

[*]Corresponding author Tel: +44 (0)20 7679 3754

Email address: `pj.tan@ucl.ac.uk` (P. J. Tan)

1. Introduction

The beneficial effects of fluid-structure interaction (FSI) in reducing the impulse imparted to a rigid free-standing plate from an underwater blast are well-known. Taylor have shown that the momentum acquired by the plate reduces dramatically with its inertial mass: a direct consequence of early cavitation at the fluid-structure interface [2]. Over the past two decades, this 'peculiar' property has been extensively exploited to design sandwich panels with a greater resistance, compared to its monolithic equivalent of the same mass, to underwater blast loadings [3–9]. However, the majority of these studies on FSI, including those on sandwich panels, have largely ignored limits to deformation - from its supports and the structural material - which could potentially limit the external validity of any model predictions. There are two important factors that influence energy and momentum transfer to a submerged structure in underwater blasts: (1) development and evolution of cavitation zone(s); and, (2) limits to material deformation, boundary (supports) compliance and its failure. In the present study, we shall be concerned only with FSI in the 'pre-boundary failure' régime, i.e. before the complete detachment of the structure from its supports.

Nomenclature

A	Cross-section area of beam	N_0	Fully plastic membrane force
B	Width of beam	N	N/N_0
c_w	Acoustic wave speed in water	p_I	Incident pressure wave
D	Damage variable	p_s	peak incident pressure
$\bar{E}^F$	Non-dimensional maximum total energy transmitted to free-standing beam	p_{R1}	Reflected pressure wave
E^T, E^K	Transmitted energy and kinetic energy of the elasto plastic beam	p_{R2}	Rarefaction pressure wave
$\bar{E}^T$, $\bar{E}^K$	Non-dimensional maximum E^T and E^K	p_{Int}	Interface pressure
E_S^b, E_S^s, E_S^m	Bending, shear, membrane energy obtained from rotational, axial and vertical springs	$\tilde{p}_{\text{Int}}$	Average interface pressure
E_B^b, E_B^s, E_B^m	Bending, shear, membrane energy of the elastoplastic beam	Q	Transverse shear force
E_i	Incident energy of blast wave per unit area	Q_0	Fully plastic shear force
H	Beam thickness	t_1, t_2, t_3	Termination time of Phases I, II and III
I_i	Incident impulse per unit area	t_c	Cavitation time
I^T, I^K	Transmitted impulse, momentum	t_i	Decay constant

3

$\bar{I}^F$	Maximum total impulse per unit area of free-standing beam	$\hat{W}$	Average transverse deflection
$\bar{I}^T$, $\bar{I}^K$	Non-dimensional maximum I^T and I^K	W_0	Maximum mid-span deflection
$\bar{I}_1^T$,	Maximum non-dimensional transmitted impulse	W_B, W_S	Deflection at mid-span & support
$\bar{I}_2^T$,	Reduction of transmitted impulse due to failure	Z	Lagrangian coordinates
$\bar{I}_3^T$,	Reduction of transmitted impulse due to deformation	β	Ratio of the plastic work absorbed through shear deformation to the total plastic work done
I^*	Non-dimensional impulse	β_c	Critical value of β separating modes II and III
$\hat{I}$	Impulse per unit area	β_w	FSI index
K_ϕ	Rotational spring stiffness	ΔW_0	Relative mid-span displacement
L	Half length of beam member	ω_d, ω_s	State variable for ductile and shear damage
L_e	Characteristic length of the first-order element in FE	$\phi_i(x)$	Admissible mode functions
L_w	Length of water column in FE	ρ	Density of beam material
M_0	Fully plastic bending moment	ρ_w	Density of water
N	Membrane force	σ_Y	Static yield strength

47

48 Treating water as a linear-elastic medium, Kennard [10] found that if the pressure at any
49 point drops below the cavitation limit, two 'breaking fronts' emerge from there and propa-
50 gate in opposite directions, creating an expanding pool of cavitated liquid. These breaking
51 fronts can arrest, invert their direction of motion and become 'closing fronts', forcing the
52 contraction of the cavitation zone. Schiffer et al. [11] studied the effects of initial hydrostatic
53 pressure on cavitation for a rigid plate with a linear backing spring. Their model is able
54 to capture the propagation of both breaking and closing fronts, as well as their interactions
55 with the structure, in a blast event. It was found that increasing hydrostatic pressure re-
56 duces the transmitted impulse since it moves the point of incipient cavitation away from the
57 structure; however, reducing inertial mass does not always lead to a reduction in the trans-
58 mitted impulse whilst increasing the supporting stiffness always will. Schiffer and Tagarielli
59 [12] further reported a 'double-cavitation' event where early plate deformation, due to the
60 propagation of flexural waves, gives rise to a localised cavitation zone at the fluid-structure
61 interface and in the central portion of the plate. This zone quickly collapses upon coales-
62 cence of the flexural wave at the centre. Subsequent plate deformation induces an additional
63 cavitation at a finite distance from the plate as previously described.

64 It is, as yet, unclear how limits to material deformation, support compliance and support fail-
65 ure affects previously known results since the impulse imparted by an underwater blast load-

4

66 ing is often sufficiently intense to induce significant plastic deformation in a structure with
67 which it interacts leading to, in extreme circumstances, a loss of structural integrity through
68 partial/complete detachment from its support. In this paper, the limitations/assumptions
69 of previous studies are relaxed by considering a fully-clamped ductile beam system - the
70 analytical framework for this was developed previously by Yuan et al. [1] in a companion
71 paper. The model of the ductile beam system is able to capture the three different modes
72 of deformation observed in blast experiments, the initiation and evolution of damage with
73 increasing transverse beam deflection, and its consequential detachment - by fracture - from
74 the supports. By coupling the fluid (water) domain to the aforesaid model of the ductile
75 beam system, the momentum and energy transferred by the blast wave are critically re-
76 evaluated for the coupled, non-impulsive loading regime; in particular, on how the beam's
77 deformation mode and boundary compliance affects the fluid and structure interaction, or
78 vice-versa, before the onset of boundary failure, defined as the complete detachment of the
79 beam from its supports.

80 The outline of this paper is as follows: Section 2 summaries the key features of the ductile
81 beam system developed in [1] and outlines the fluid-structure coupling strategy; details
82 of the three-dimensional (3D) FE model are given in Section 3; Section 4 compares the
83 predictions of the analytical and FE models; and, finally, results for the elasto-plastic and
84 rigid free-standing beams are compared and sensitivity analyses carried out to elucidate the
85 dependence of the model predictions on the beam's aspect ratio and inertial mass in Section
86 5.

2. Analytical model [1]

88 The analytical framework for the fully-clamped ductile beam system - developed by Yuan
89 et al. [1] in a separate study - are briefly outlined with particular attention paid to high-
90 lighting the key elements that had been introduced to incorporate elasto-plastic constitutive
91 behaviour, boundary compliance and boundary failure. This is followed by details on cou-
92 pling strategy between the fluid domain and beam system, and on the limitations of the
93 current FSI model.

2.1. Fully clamped ductile beam system - key features

95 The ductile beam system incorporates the following: (1) large elasto-plastic deformation
96 with catenary action; (2) interactions between bending, membrane stretch and transverse
97 shear; and, (3) limits to deformation through a loss of integrity at the support and the
98 subsequent beam detachment by rupture. Figure 1 shows a schematic of the slender beam
99 supported at each end by three springs (one rotational and two axial). The pressure loading
100 $p(x, t)$ is assumed to always impinge normally over the span of the beam regardless of its
101 subsequent transverse deflection [13, 14]. Hence, a plane of geometric and loading symmetry
102 exists at the mid-span of the beam ($x = 0$), allowing one-half of the beam to be analysed.

5

The beam - made of a rate-independent, elastic perfectly-plastic material - has a total length $2L$ and a uniform rectangular cross-section of thickness H and width B where $L/H \gg 1$. The rotational spring has elasto-plastic characteristics to model the end rotation of the beam and the subsequent formation of a plastic hinge. Both the axial and vertical springs have rigid-plastic characteristics to model the 'plastic stretch' and 'plastic shear sliding' actions at the support, respectively.
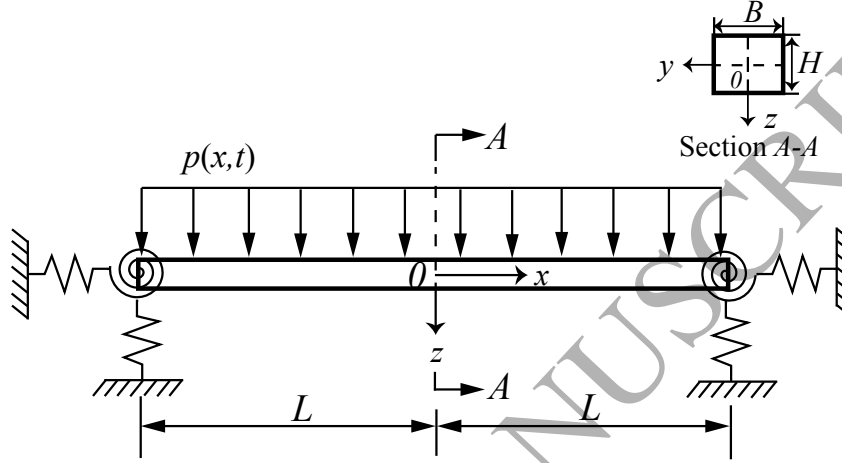

Figure 1: Schematic of the fully clamped ductile beam system by Yuan et al. [1]. A plane of symmetry exists along $x = 0$, $-B/2 \leq y \leq B/2$, $-H/2 \leq z \leq H/2$ so that only the right-half needs to be analysed.

2.1.1. Fully plastic stress condition, damage and failure criteria

Plastic limit function, damage and failure criteria are first established as functions of non-dimensional fully plastic generalised stresses, viz. $\bar{M}(\triangleq M/M_0)$, $\bar{N}(\triangleq N/N_0)$ and $\bar{Q}(\triangleq Q/Q_0)$ where $M_0 = \sigma_Y BH^2/4$, $N_0 = \sigma_Y BH$ and $Q_0 = \sigma_Y BH/\sqrt{3}$ are the fully plastic bending moment, membrane force and transverse shear force, respectively; and, σ_Y is the uniaxial static yield strength of the beam material. For a beam of rectangular cross-section, its fully plastic limit function ψ^p can be written as [15]

$$\psi^p = |\bar{M}|\sqrt{1 - \bar{Q}^2} + \bar{N}^2 + \bar{Q}^2 - 1. \tag{1}$$

Consequently, a plastic hinge forms at any cross section where the fully plastic stress condition $\psi^p = 0$ is reached.

Damage shall refer to the onset and subsequent degradation of the generalised stresses in the beam or its supports, or both. Figure 2 gives a schematic of the variation of generalised stresses $(\bar{M}$ or $\bar{N}$ or $\bar{Q})$ versus effective strain ϵ_{eff} defined on any cross section of the beam, including at its supports. Point c denotes the generalised stress state at a cross-section when the damage initiation criterion is satisfied as follows:

$$\omega_d = \frac{\epsilon_{\text{eff}}}{\epsilon_d} = 1 \tag{2}$$

6

where ω_d is a state variable that increases monotonically with effective strain ϵ_{eff}, and ϵ_d is
the effective strain corresponding to the onset of damage. Beyond this, progressive softening
of the non-dimensional generalised stresses occur in accordance to

$$|\bar{M}| = |\bar{M}^f|(1 - D), \quad \bar{N} = \bar{N}^f(1 - D) \quad \text{and} \quad \bar{Q} = \bar{Q}^f(1 - D) \tag{3}$$

where D is a damage variable; $\bar{M}^f$, $\bar{N}^f$ and $\bar{Q}^f$ are the non-dimensional bending moment,
membrane force and transverse shear force at the onset of damage, respectively. For sim-
plicity, a linear evolution of the damage variable D with effective strain ϵ_{eff} is adopted as
follows [16]:

$$D = \frac{\epsilon_{\text{eff}} - \epsilon_d}{\epsilon_r - \epsilon_d} \tag{4}$$

where ϵ_r is the rupture strain to be obtained from a uniaxial tensile test. This definition
ensures that all the generalised stresses reduce to zero when $D = 1$.
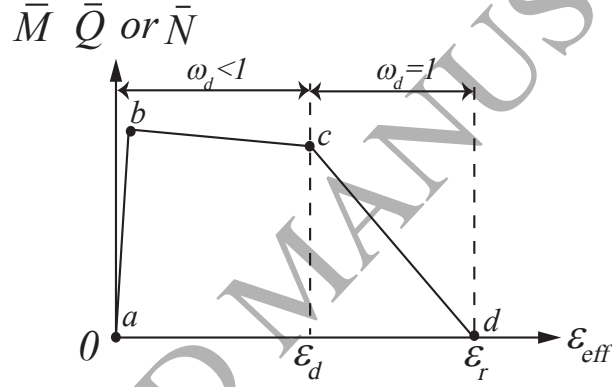

Figure 2: Schematic on how the non-dimensional generalised stresses vary with effective strain pre- ($\omega_d < 1$)
and post- ($\omega_d = 1$) damage initiation.

Failure refers to a complete loss of load carrying capacity by the beam through detachment
from its supports. Since the effective strain ϵ_{eff} is always greatest at the support ($x = L$) -
see Section 2.1.2 - a *failure* criterion needs only to be defined there where damage must first
initiates and where failure would subsequently occur [17, 18]. The criteria delineating the
different modes of failure, corresponding to those previously identified by Menkes and Opat
[19], are as follows:

$$\text{Mode I}: \quad D < 1, \quad \omega_s < 1 \tag{5a}$$

$$\text{Mode II}: \quad D = 1, \quad \omega_s < 1 \tag{5b}$$

$$\text{Mode III}: \quad D = 1, \quad \omega_s \geq 1. \tag{5c}$$

The state variable ω_s is expressed as

$$\omega_s = \frac{\beta}{\beta_c} \tag{6}$$

7

133 where β is the ratio of the plastic work absorbed through shearing deformation to the total
134 plastic work done by all the other stress components given by [20]

$$\beta = \frac{E_S^s}{E_S^s + E_S^b + E_S^m} \tag{7}$$

135 where E_S^s is the shear strain energy (vertical axial spring); E_S^b is the bending strain energy
136 (rotational spring); E_S^m is the membrane strain energy (horizontal axial spring); and, β_c is
137 the critical β value delineating the transition from mode II to III to be given later.

2.1.2. Effective strain ϵ_{eff} and material properties

139 The effective strain ϵ_{eff} in Eqs. 2 and 4 will now be approximated. In general, the effective
140 strain ϵ_{eff} on any cross-section is given by [17, 18]

$$\epsilon_{\text{eff}} = \sqrt{\frac{2}{9}\Big[(\epsilon_{xx} - \epsilon_{yy})^2 + (\epsilon_{yy} - \epsilon_{zz})^2 + (\epsilon_{xx} - \epsilon_{zz})^2 + \frac{3}{2}(\gamma_{xz}^2 + \gamma_{zy}^2 + \gamma_{xy}^2)\Big]}. \tag{8}$$

141 For slender member where its thickness H is much smaller compared to its half-length L,
142 out-of-plane warping of cross-section is negligible; hence, plane sections remain plane [15].
143 Therefore, it is reasonable to write $\gamma_{xy} = \gamma_{yz} = 0$ [17, 18]. If the material in a dynamic
144 uniaxial test where $\epsilon_{xx} > 0$ obeys the incompressibility relation $\epsilon_{xx} + \epsilon_{yy} + \epsilon_{zz} = 0$, then
145 $\epsilon_{yy} = \epsilon_{zz} = -\epsilon_{xx}/2$ [21]. Thus, Eq. 8 simplifies to

$$\epsilon_{\text{eff}} = \sqrt{\epsilon_{xx}^2 + \frac{1}{3}\gamma_{xz}^2}. \tag{9}$$

146 The maximum total in-plane strain ϵ_{xx} on any cross-section x comprises of two parts given
147 by [17, 21]

$$\epsilon_{xx} = \epsilon_m + \epsilon_b \tag{10}$$

148 where the membrane strain ϵ_m and bending strain ϵ_b may be expressed, respectively, as
149 functions of the transverse mid-span displacement of the beam W_B as follows:

$$\epsilon_m = 2\Big(\frac{W_B}{L}\Big)^2\Big(\frac{x}{L}\Big)^2 \tag{11}$$

150 and

$$\epsilon_b = \frac{W_B H}{L^2}. \tag{12}$$

151 Just as in [21], a linear variation of the membrane strain ϵ_m along the half-length of the
152 beam is also assumed here for simplicity.

153 Following [17, 18, 22, 23], the transverse shear strain γ_{xz} is neglected in the beam member
154 whist, at the support, it depends on the plastic shear sliding distance over the shear band.
155 Thus, on any cross-section of the ductile beam, it follows that

$$\gamma_{xz} = \begin{cases} 0 & \text{if } 0 \leq x < L \\ W_S/(l/2) & \text{if } x = L \end{cases} \tag{13}$$

156 where W_S is the plastic shear sliding displacement and l is the width of the shear band.
157 Slip-line field analysis of a rigid-plastic beam with rectangular cross-section and thickness H
158 by Nonaka [24] showed that the width of the shear band ranges between $H \leq l \leq 2H$ if the
159 maximum transverse beam deflection is between 0 to H. The latter $(l = 2H)$ corresponds
160 to the onset of membrane (or catenary) response in the beam. Since large beam deflection
161 invariably leads to membrane effects, a value of $l = 2H$ is adopted here by following [23, 25].
162 Substituting Eqs. 10 - 13 into Eq. 9, gives an approximate expression for the effective strain
163 on any cross-section x of the beam system as follows:

$$
\epsilon_{\text{eff}} = \begin{cases} 2\left(\frac{W_B}{L}\right)^2 \left(\frac{x}{L}\right)^2 + \left(\frac{W_B H}{L^2}\right) & \text{if } 0 \leq x < L \\ \sqrt{\left[2\left(\frac{W_B}{L}\right)^2 + \left(\frac{W_B}{L}\right)\left(\frac{H}{L}\right)\right]^2 + \frac{1}{3}\left(\frac{W_S}{H}\right)^2} & \text{if } x = L \end{cases}.
$$
(14)

164 It is worth re-emphasising that the effective strain is always greatest at the supports $(x = L)$
165 since its two constituent components (total in-plane ϵ_{xx} and transverse shear strains γ_{xz})
166 are both highest there; this is also in agreement with results in [17, 18]. Expressions for W_B
167 and W_S are to be derived later in Section 2.1.3.

168 Table 2 lists the material properties for Aluminium 6061-T6 beams used by Menkes and
169 Opat [19]; they may be assumed to be strain rate insensitive [26]. In this study, we adopt a
170 rupture strain of $\epsilon_r = 0.5$ [20] and an effective strain corresponding to the onset of damage
171 at $\epsilon_d = 0.38$ - both were calibrated to the experimental data of Menkes and Opat [19].
172 Yu and Chen [22] have previously shown that β_c obtained for a square yield criterion is
173 greater than that obtained for an interactive yield criterion $(\beta_c = 0.45)$ by Shen and Jones
174 [20]. Furthermore, they established that β_c is a material-dependent parameter which is
175 independent of geometry. Since the present study adopts an interactive fully plastic limit
176 function and the same material properties as [20, 22] were used, it is reasonable to adopt
177 $\beta_c = 0.45$.

Table 2: Material properties for the Aluminium 6061-T6 beam [19]

Density, ρ (kg/m^3)	Young's modulus, E (GPa)	Static yield stress, σ_Y (MPa)	Poisson's ratio
2686	69	283	1/3

178 *2.1.3. Equations of motion*

179 Following [13, 14, 27], the deformation of the beam is divided into three phases - see Fig. 3
180 - according to the sequence of plastic hinge formation as follows: (1) Phase 1 $(0 < t \leq t_1)$ -
181 when plastic hinge does not form (or the fully plastic stress condition is not met) anywhere
182 in the beam, i.e. $\psi^p < 0$; (2) Phase II $(t_1 < t \leq t_2)$ - when a stationary plastic hinge forms
183 at the support; (3) Phase III $(t_2 < t \leq t_3)$ - when a travelling plastic hinge A moves towards,

9

(a) $0 < t \leq t_1$

(b) $t_1 < t \leq t_2$
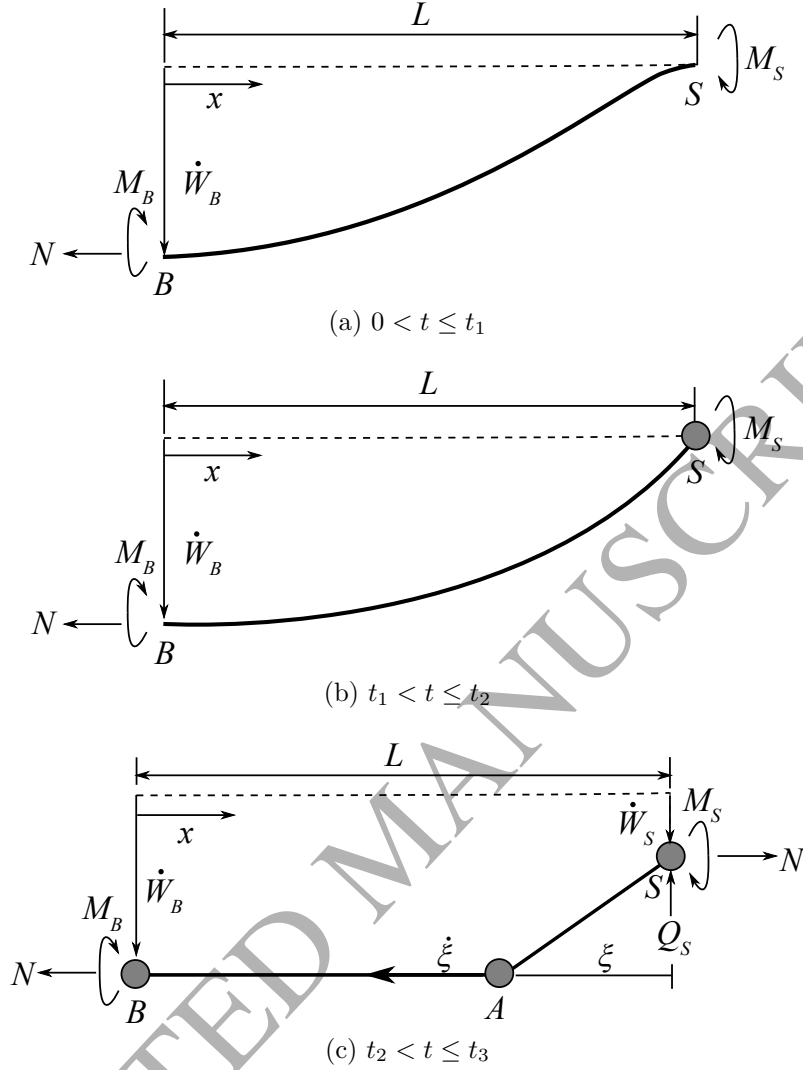
(c) $t_2 < t \leq t_3$

Figure 3: Schematic of the transverse displacement profile for the right-half of the ductile beam system in [1] : (a) Phase I, (b) Phase II and (c) Phase III.

and coalesce with, the existing stationary hinge at the mid-span of the beam, ending up in a final two-hinge collapse configuration.

In each phase, the transverse displacement of the beam at a point x $(x > 0)$ along the beam member and at its support is approximated as a sum of n generalised displacements and mode functions given by [28]

$$W(x,t) = \sum_{i=1}^{n} \phi_i(x) w_i(t) \tag{15}$$

where the partial functions $\phi_i(x)$ are admissible mode functions that satisfy the geometric boundary conditions and the temporal functions $w_i(t)$ are generalised transverse displace-

10

¹⁹¹ ments. The displacement at the mid-span and supports are, respectively,

$$W_B(t) = W(x = 0, t) \quad \text{and} \quad W_S(t) = W(x = L, t). \tag{16}$$

¹⁹² The corresponding velocity ($\dot{W}$) and acceleration ($\ddot{W}$) fields also uses the same partial func-
¹⁹³ tions given by

$$\dot{W}(x, t) = \sum_{i=1}^{n} \phi_i(x)\dot{w}_i(t) \quad \text{and} \quad \ddot{W}(x, t) = \sum_{i=1}^{n} \phi_i(x)\ddot{w}_i(t). \tag{17}$$

¹⁹⁴ The differential equations governing w_i can be obtained by substituting the *Lagrangian*
¹⁹⁵ ($\triangleq E_k + V$ where E_k and V is total kinetic and potential energy of the system, respectively)
¹⁹⁶ for the structural beam system into the well-known Lagrange equation of the 2nd kind, and
¹⁹⁷ simplifying, to give [1]

$$\sum_{j=1}^{n} M_{ij}\ddot{w}_j + \frac{\partial V}{\partial w_i} = \int_0^L p(x, t)\phi_i(x)\mathrm{d}x, \quad i = 1, 2, ..., n \tag{18}$$

¹⁹⁸ where M_{ij} is the generalised mass given by

$$M_{ij} = \begin{cases} m \int_0^L \phi_i(x)\phi_j(x)\mathrm{d}x & \text{if } i \neq j \\ m \int_0^L \phi_i^2(x)\mathrm{d}x & \text{if } i = j \end{cases}, \tag{19}$$

¹⁹⁹ m is the mass per unit length; $V (\triangleq E_S^b + E_S^s + E_S^m + E_B^b + E_B^m)$ is the total potential energy
²⁰⁰ of the beam system; E_B^b and E_B^m are the bending and membrane strain energies of the beam
²⁰¹ member, respectively; E_S^s, E_S^b and E_S^m are the shear, bending and membrane strain energies
²⁰² associated with the vertical, rotational and axial springs, respectively, at the supports. Note
²⁰³ that subscripts S and B denote support and beam member, respectively; whilst, superscripts
²⁰⁴ s, b and m denote shear, bending and membrane, respectively. The key to obtaining the
²⁰⁵ governing equations of motion in Eq. 18 is to derive the various strain energy components
²⁰⁶ (E_S^b, E_S^s, E_S^m, E_B^b and E_B^m) for each Phase – they are summarised in Appendix A.

²⁰⁷ *2.2. Coupling of fluid domain to the structure*

²⁰⁸ Consider a rightward-propagating planar pressure pulse that travels at a constant speed
²⁰⁹ $c_w (=1498$ m/s) in a fluid of density $\rho_w (=1000$ kg/m³), and impinging normally on the
²¹⁰ structural beam system shown schematically in Fig 4. It is convenient to define a spatial
²¹¹ coordinate Z in the un-deformed configuration with $Z = 0$ corresponding to the location of
²¹² the fluid and structure interface, i.e. $Z = z + H/2$. Assuming an exponentially decaying
²¹³ blast pulse with a peak pressure p_s and time constant t_i, then the incident pressure wave at
²¹⁴ any arbitrary point (of coordinate Z and x) at the time t may be expressed as [2]

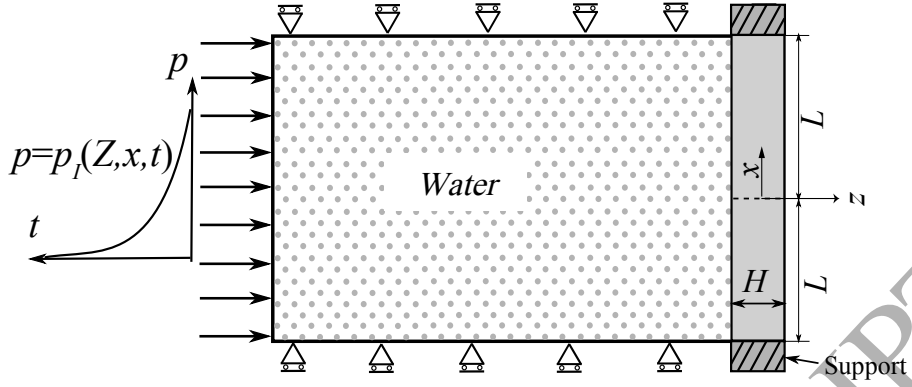$$p_I(Z, t) = p_s e^{-(t - Z/c_w)/t_i}. \tag{20}$$

Figure 4: Schematic of an exponentially decaying wave propagating to the right towards a clamped elasto-plastic beam system.

The incident pulse duration is considered to be infinitely long, i.e. $t_d = \infty$. If the target structure is rigid and fixed in space, then the reflected wave would be

$$p_{R1}(Z,t) = p_s e^{-(t+Z/c_w)/t_i} \tag{21}$$

corresponding to a perfect reflection of the incident wave in the negative Z direction. Since the beam is not rigid, the impingement of the incident pressure wave on this interface sets the beam in motion, i.e. the beam acquires a velocity field $\dot{W}(x,t)$. Compatibility dictates that the wetted surface of beam and the fluid particles at its interface possess the same velocity $\dot{W}(x,t)$, provided cavitation is absent (everywhere) at the fluid and structure interface. The beam motion results in a rarefaction wave (travelling in negative Z-direction) of magnitude

$$p_{R2}(Z,x,t) = -\rho_w c_w \dot{W}(x, t + Z/c_w). \tag{22}$$

It is worth emphasising that the reflection of planar waves off a curved interface would render the exact formulation of the fluid pressure field too complicated to quantify. As a simplification, the reflected waves are treated as planar and propagates in the negative Z-direction, without affecting the pressure and particle velocity fields perpendicular to the incident angle. Thus, the net water pressure $p(Z,x,t)$ due to the incident and reflected pulses is given by

$$p(Z,x,t) = p_I + p_{R1} + p_{R2} = p_s \left[e^{-(t-Z/c_w)/t_i} + e^{-(t+Z/c_w)/t_i} \right] - \rho_w c_w \dot{W}(x, t + Z/c_w). \tag{23}$$

The interface pressure (at $Z = 0$) is, therefore,

$$p_{\text{Int}}(x,t) = p(Z = 0, x, t) = 2p_s e^{-t/t_i} - \rho_w c_w \dot{W}(x,t). \tag{24}$$

Substituting $p_{\text{Int}}(x,t)$ into Eq. 18 and rearranging gives the governing ordinary differential equations that describes the beam motion as follows:

$$\sum_{j=1}^{n} M_{ij} \ddot{w}_j + \frac{\partial V}{\partial w_i} = B \int_0^L p_{\text{Int}}(x,t)\phi_i(x)\mathrm{d}x, \quad i = 1, 2, ..., n. \tag{25}$$

12

2.3. Limitations of the current FSI model

The tensile term (p_{R2} in Eq. 22) may, under certain circumstances, causes the fluid pressure to drop below zero at some point in time within the fluid domain, giving rise to a cavitation event. Following cavitation, the pressure field in the fluid is given by a superposition of two breaking fronts, one travelling towards the structure (positive Z direction) and the other away (negative): generating an expanding pool of cavitated liquid [10]. Schiffer et al. [11] identified two cavitation types (or régimes) for underwater blast loading of rigid-plate with a linear backing spring that depends on the fluid conditions in the layer between the structure and the expanding cavitation zone. *Type I* cavitation occurs if a breaking front (travelling in the positive Z direction), arrests before reaching the fluid-structure interface, reverses its motion and becomes a closing front. *Type II* cavitation occurs if the breaking front (travelling in positive Z direction) reaches the fluid-structure interface and causes cavitation at the interface. In the present study, *Type II* cavitation will occur if the condition [11]

$$p_{\text{Int}}(x, t) = 0 \tag{26}$$

is met. Since Schiffer et al. [11] showed that a structure acquire s greater transmitted impulse in *Type I* than in *Type II*, the former would be of greater interests to a designer since the objective of this work is concerned with the limits of structural and material deformation.

In a *Type I* cavitation, several authors [11, 12] had found that the pressure wave (rarefaction p_{R2} and reflected p_{R1}) emanating from the fluid-structure interface approaches the closing front and eventually reflects back towards the fluid-structure interface as a positive pressure pulse. It was noted in [11] that this positive pressure pulse acts continuously on their rigid plate which reduces to zero after a finite duration. As a consequence, it must contribute to the impulse transmitted to the structure and in cases where the mass and stiffness of the structure are high, the maximum transmitted impulse can even exceed twice the incident impulse $I_i = p_s t_i$. However, detailed three-dimensional (3D) finite element simulations (to be presented later in Section 4) will show that for elasto-plastic beams deforming in any modes of deformation, the contribution of the reflection wave (from the closing front) during *Type I* cavitation does not significantly affect the maximum mid-span deflection, maximum momentum, maximum transmitted impulse, maximum kinetic energy and maximum transmitted energy to the beam. On this basis, it is reasonable to neglect the influence of the reflection wave from the closing front in the current analytical model.

3. Finite element (FE) model

In addition to the analytical model presented above, three-dimensional (3D) FE calculations were also performed - using the commercial software ABAQUS/ Explicit® - to model the fluid-structure interaction. Here, only the salient features of the FE model set-up are presented for the fully-clamped beam since they are described previously in Yuan et al. [1]. Details on convergence studies and validation are found there.
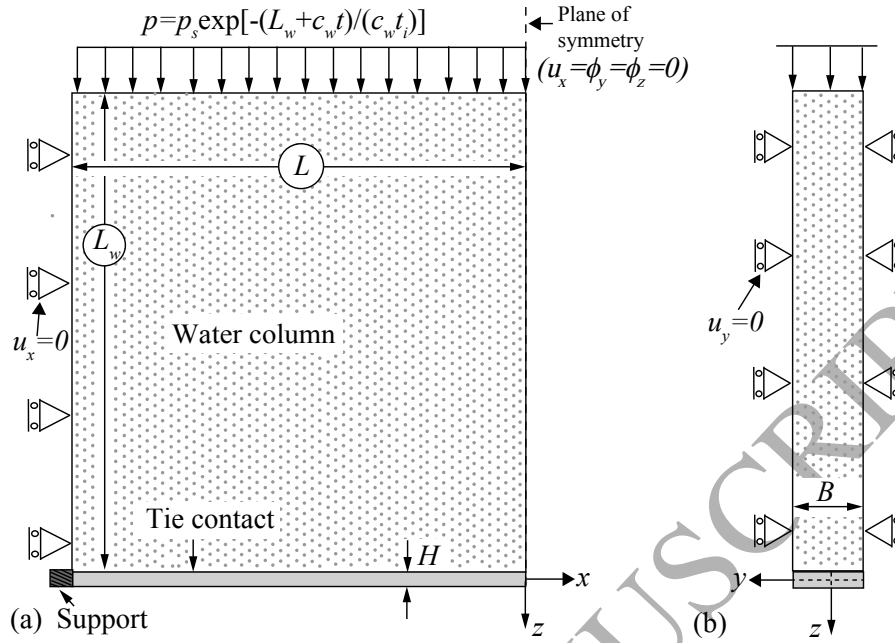
13

Figure 5: Schematic of clamped beam subjected to an exponentially decaying pressure pulse in FE: (a) front view and (b) side view.

3.1. Material properties and damage model

Material description based on the conventional J_2 flow theory is adopted to allow progressive degradation of material stiffness to be implemented in finite elements. This approach, coupled with element deletion, is widely used to model progressive damage and rupture of ductile materials [29, 30]. All the beams modelled are made of Aluminium 6061-T6 - the material properties are given in Table 2. The progressive damage model for ductile materials in ABAQUS/Explicit is adopted here. The criterion for ductile damage initiation is given by

$$\omega_d = \int \frac{d\bar{\epsilon}^p}{\bar{\epsilon}^p_d(\eta, \dot{\bar{\epsilon}}^p)} = 1 \tag{27}$$

where ω_d is a state variable that increases monotonically with the equivalent plastic strain. Here, the equivalent plastic strain $\bar{\epsilon}^p_d$ at the onset of ductile damage is a function of stress triaxiality η and plastic strain rate $\dot{\bar{\epsilon}}^p$ [31]. When Eq. 27 is met, the damage variable D would increase according to [16]

$$\dot{D} = \frac{L_e \dot{\bar{\epsilon}}^p}{\bar{u}^p_f} \tag{28}$$

where $\bar{u}^p_f$ is the effective plastic displacement at failure and $L_e = 7.83 \times 10^{-4}$ m is the characteristic length of the first-order element used in the FE model - this is identical to that in [1]. Any element whose stiffness is fully degraded, i.e. $D = 1$, is deleted from the mesh. The two parameters needed to implement a ductile damage model are the damage

14

279 strain $\bar{\epsilon}_d^p = 0.8$ and the failure displacement $\bar{u}_f^p = 1.1 \times 10^{-3}$ m; both were obtained through
280 calibration to the experimental data by Menkes and Opat [19].

281 The water is modelled as an acoustic medium with density $\rho_w = 1000$ kg/m^3, wave speed
282 $c_w = 1498$ m/s and bulk modulus $E_w = 2.244$ GPa. It can be treated as linear elastic under
283 compression, with zero tensile strength and zero shear modulus. A Mie-Gruneisen equation
284 of state with a linear Hugoniot relation is used to model the linear elastic ratio between
285 applied pressure $p(Z,t)$ and volumetric strain ϵ_V given by

$$p(Z,t) = \begin{cases} -E_w\epsilon_V = -c_w^2\rho_w\epsilon_V, & \epsilon_V < 0 \\ 0, & \epsilon_V \geq 0 \end{cases} . \tag{29}$$

286 Note that when $\epsilon_V \geq 0$, the pressure becomes zero and this leads to an onset of cavitation
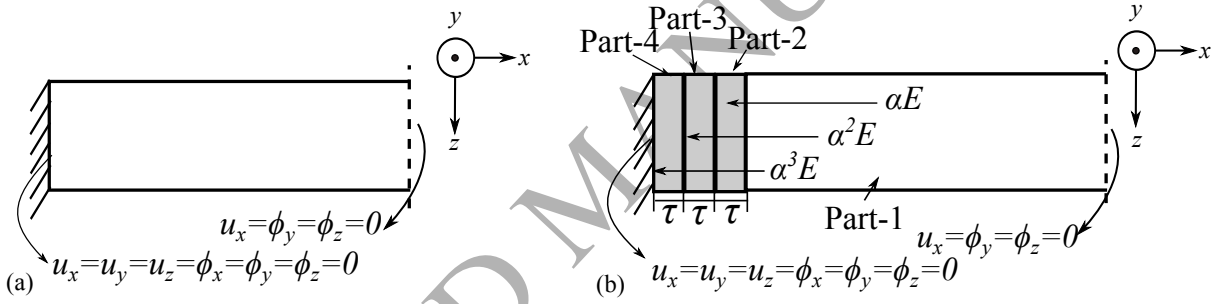287 [3, 4, 32].

3.2. Mesh, loading and boundary conditions

Figure 6: Schematic of boundary, or support, conditions (BCs) in the FE simulations: (a) standard fully clamped BC and (b) modified BC. u and ϕ denote displacement and rotation degree of freedom, respectively.

289 The FE model, shown schematically in Fig 5, consists of a water column $L_w \times L \times B$ above
290 the elasto-plastic beam. Only one-half of the fully-clamped beam and water column are
291 modelled since reflected symmetry exists on the plane bounded by $x = 0$, $-B/2 \leq y \leq B/2$
292 and $-H/2 - L_w \leq z \leq H/2$. Figure 6a depicts the standard displacement boundary
293 conditions that would need to be imposed for a fully-clamped boundary condition (BC).
294 It has been shown in [1] that the local equivalent plastic strain in the beam abutting the
295 supports does not converge with repeated mesh refinement. In order to accurately model
296 progressive ductile fracture /rupture at the supports, a modified BC given in Fig 6b is
297 adopted. Yuan et al. [1] showed that both the standard and modified BCs predict similar
298 beam deflection profiles, but only the latter gives a converged equivalent plastic strain at the
299 boundary/support. A similar procedure was also adopted by Yuan and Tan [33] to model the
300 impulsive response of rectangular plates numerically. For the modified BC, three additional
301 parts (labelled 2-4) are added to the end of the original solid beam (part-1) to form an
302 extended boundary shown schematically in Fig 6b. Note that the standard fully-clamped
303 BC of Fig 6a is imposed on part 4. All the additional parts have equal width τ and identical

15

304 material properties as the solid beam, apart from a gradation of their elastic modulus E,
305 by a factor α. The parameters $\tau = H/6$ and $\alpha = 10$ were obtained by calibration to the
306 experimental data of [19] - the details are provided in Yuan et al. [1].

307 Horizontal displacement u_x for the left boundary of the water column ($u_x = 0$ at $x = -L$,
308 $-B/2 \leq y \leq B/2$, $-H/2 - L_w \leq z \leq -H/2$) is constrained as does the vertical displacement
309 u_y on the front ($u_y = 0$ at $-L \leq x \leq 0$, $y = B/2$, $-H/2 - L_w \leq z \leq -H/2$) and back
310 ($u_y = 0$ at $-L \leq x \leq 0$, $y = -B/2$, $-H/2 - L_w \leq z \leq -H/2$) boundary of the water
311 column - see Fig 5. An exponentially decaying pressure pulse, given by Eq. 20, is applied
312 to the top of the water column. Tie constraints are applied between the wetted edge of the
313 beam and fluid.

314 The half-beam modelled has a dimension of 0.06 m (L) $\times$ 0.01 m (H) $\times$ 0.01 m (B).
315 The length of water column L_w is sufficient long to ensure the reflected wave from the top
316 boundary does not reach the structure over the duration of the calculation [3, 4]. $L_w/c_w t_i = 3$
317 is used to ensure that the water column is semi-infinite. Both the beam and water column
318 are discretised using the 8-noded solid elements (C3D8R) with reduced integration and
319 hour-glass control. In order to capture necking localisation, progressive damage and ductile
320 fracture with acceptable fidelity, twelve elements are used through the beam thickness (H).
321 Results of convergence studies have shown this to be sufficient. All C3D8R elements - used
322 to discretise the water column and beam - are cubic in size with a dimension of 7.83×10^{-4} m;
323 consequently, the nodes of the water and solid meshes are coincident at the fluid-structure
324 interface.

325 4. Comparison of analytical and FE predictions

To assess the fidelity of the analytical model, its predictions for the average interface pressure,
mid-span deflection, impulse and energy transfer will now be compared to predictions by the
FE model. Appendix A gives all the energy expressions for the three phases of deformation
and a flow chart on the numerical implementation of the analytical model is presented in
Section 2. The temporal history of the transmitted impulse per unit area $I^T(t)$, momentum
per unit area $I^K(t)$, transmitted energy per unit area $E^T(t)$ and kinetic energy per unit area
$E^K(t)$ of the beam are defined, respectively, as follows:

$$I^T(t) = \int_0^t \tilde{p}_{\text{Int}}(t)\mathrm{d}t, \quad I^K(t) = \frac{\rho H}{L}\int_0^L \dot{W}(x,t)\mathrm{d}x,$$
$$E^T(t) = \frac{1}{BL}\int_0^L p_{\text{Int}}(x,t)W(x,t)\mathrm{d}x, \quad E^K(t) = \frac{\rho H}{2L^2}\int_0^L \dot{W}^2(x,t)\mathrm{d}x. \quad (30)$$

326 Note that the average interface pressure is given by

$$\tilde{p}_{\text{Int}}(t) = \frac{1}{L}\int_0^L p_{\text{Int}}(x,t)\mathrm{d}x. \tag{31}$$

16

327 Time t is measured from the instant when the incident pressure wave arrives at the fluid
328 and structure interface. The impulse and energy components in Eq. 30 are normalised by
329 the incident impulse per unit area I_i and incident energy per unit area E_i given by [2]

$$I_i = p_s t_i \quad \text{and} \quad E_i = p_s^2 t_i / \rho_w c_w. \tag{32}$$

330 Unless otherwise specified, a time constant of $t_i = 0.2$ ms - corresponding to 16 kg of
331 TNT at a 1.4 m standoff distance according to the scaling law by Swisdak [34] - was used
332 in all calculations; consequently, variations of FSI index β_w is achieved by altering the
333 beam thickness. It is worth emphasising that in both analytical and FE model, if the
334 structural system fails (i.e. complete detachment occurs) before all the initial kinetic energy
335 is expended, then the beam member would have a residual kinetic energy at the point
336 of severance. Parts of this are absorbed through further plastic deformation as the beam
337 member continues to deform until it reaches a rigid permanent set whilst the remaining as
338 translational kinetic energy. Since fluid-structure interaction in the 'pre-detachment' régime
339 is of interests, the energy (and impulse) transferred 'post-detachment' by the blast wave is
340 not considered, or characterised, here.

341 Figures 7a, 7b and 7c compare the analytical and FE predictions for beams that deform in
342 mode I, II and III, respectively. Pressure contour plots predicted by FE (to be presented
343 later in Fig 8) confirm that a *Type I* cavitation event (i.e. the breaking front travelling in
344 the positive Z-direction, always arrests before it reaches the fluid-structure interface and
345 inverts its motion as a closing front) occurs in all the cases shown in Figs 7a, 7b and 7c
346 at $t_c/t_i = 0.53$, $t_c/t_i = 0.41$ and $t_c/t_i = 0.36$, respectively. For beams deforming in mode
347 I, Figure 7a shows that their non-dimensional average interface pressure $\tilde{p}_{\text{Int}}/p_s$ initially
348 decreases before attaining a peak value at time $t = t_3$ (when the beam reaches its maximum
349 mid-span deflection); this is followed by a monotonic reduction in interface pressure. Beyond
350 $t > t_3$, the FE model predicts that $\tilde{p}_{\text{Int}}/p_s$ remains positive - this is in agreement with [11].
351 The analytical model under-predicts the maximum transmitted impulse in mode I by up
352 to 12.7% since it neglects the additional loading from the reflected wave arising from the
353 closing front. Complete detachment occurs shortly after cavitation in Figs 7b and 7c which
354 explains why it is acceptable to neglect the effects of the reflected wave from the closing
355 front in the subsequent structural response. In general, the predicted interface pressure,
356 mid-span deflection, impulse and energy exchange are in good agreement with those from
357 FE for all three modes of deformation.

358 The impulse and energy transferred to the beam through FSI, also plotted in Fig 7, can
359 be succinctly summarised as follows: (1) In mode I, the average interface pressure beyond
360 $t > t_3$ does not further contribute to the transmitted energy E^T. This is because the beam
361 now responds in an elastic manner with deflection that decreases slightly before reaching
362 permanent set; (2) In modes II and III, both the transmitted impulse I^T and transmitted
363 energy E^T reach a maximum at $t = t_3$ following complete detachment from the supports;
364 (3) The maximum momentum I^K and kinetic energy E^K are reached before the onset of
365 cavitation at $t = t_c$ for all three modes, this also agrees with analytical predictions in [11];
366 (4) The maximum transmitted impulse is significantly higher in mode I than in modes II
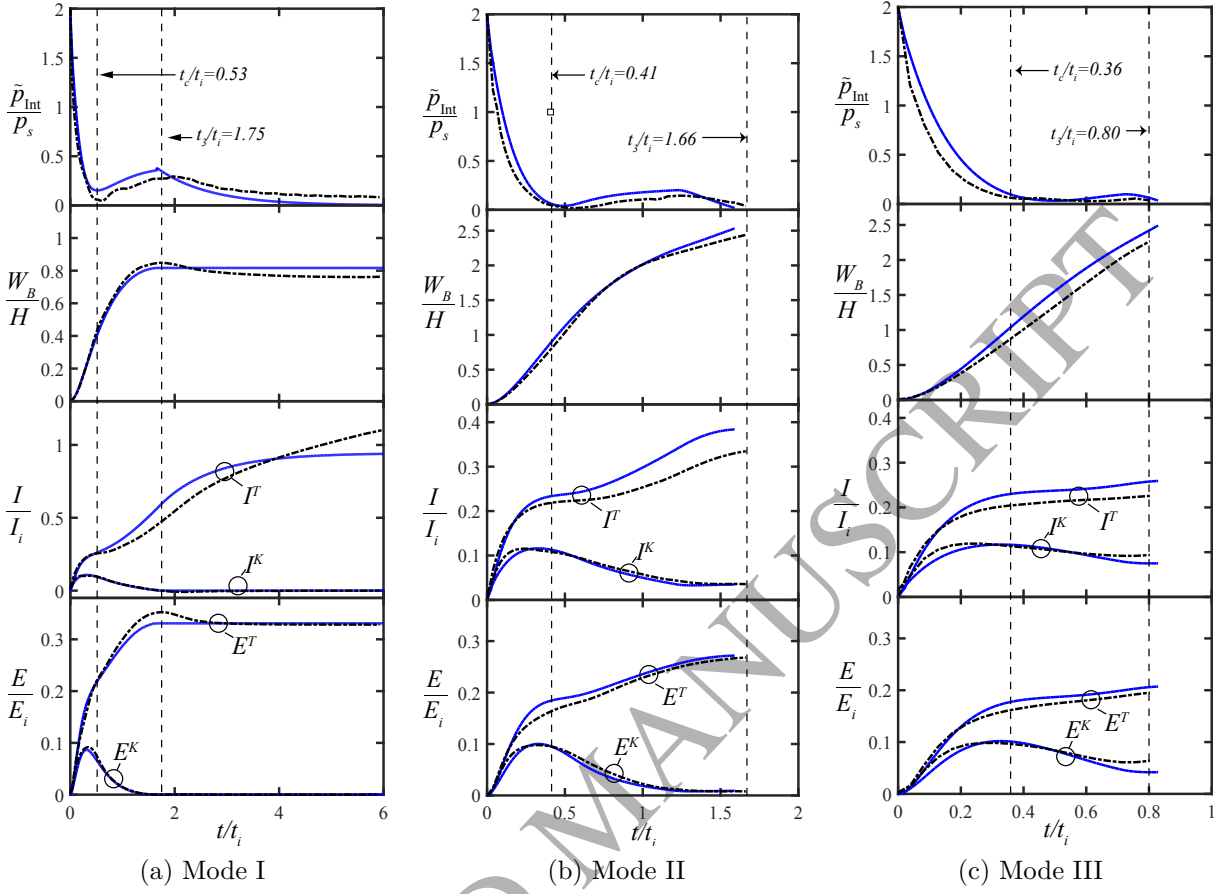
17

Figure 7: Analytical and FE predictions of the non-dimensional interface pressure, mid-span deflection, impulse transfer and energy exchange for 0.06 m (L) × 0.01 m (H) × 0.01 m (B) ($L/H = 6$ and $\beta_w = 10.9$) beam deforming in different modes subjected to three different exponentially decaying pressure pulses of identical time constant $t_i = 0.2$ ms and a peak pressure of (a) $p_s = 30$ MPa, (b) $p_s = 80$ MPa and (c) $p_s = 110$ MPa. — current analytical predictions; -.- current FE predictions. t_c and t_3 denote the time when cavitation first occurs and when the beam reaches its maximum transverse deflection, respectively.

367 and III because a considerable amount of impulse is transmitted to the beam during elastic
368 rebound; and, (5) The maximum transmitted impulse and energy are higher in mode II than
369 III since t_3 for mode III is smaller than mode II.

370 To gain an insight into the cavitation event, pressure contour maps predicted by detailed 3D
371 FE simulations are plotted in Fig 8 at five selected times (corresponding to the elasto-plastic
372 beam and loading parameters of Fig 7). Here, only the results for a third of the 'water-tank',
373 i.e. $L_w/3$, is plotted. It is worth emphasising that cavitation first occurs at $t_c/t_i = 0.53$
374 (for mode I), $t_c/t_i = 0.41$ (for mode II) and $t_c/t_i = 0.36$ (for mode III). This is caused by
375 the tensile wave (Eq. 22) which is generated as a consequence of the rapid motion of the
376 beam and is reminiscent of the experimental observations made in [12] for circular plates.
377 All the cases shown in Fig 8 correspond to a *Type I* cavitation event since the breaking
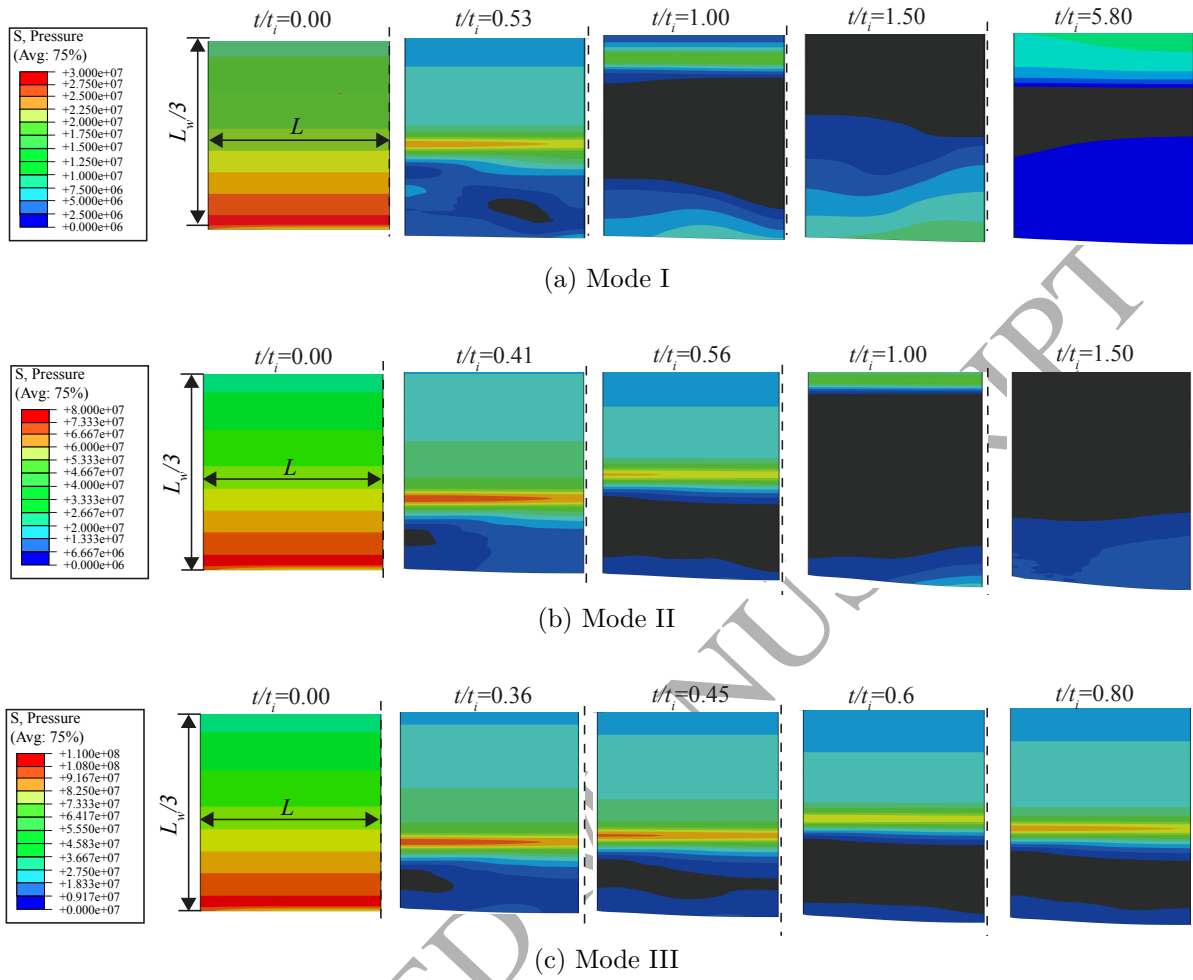
18

(a) Mode I

(b) Mode II

(c) Mode III

Figure 8: FE predictions of fluid pressure field at five selected times corresponding to the cases ($L/H = 6$ and $\beta_w = 10.9$) shown in Figs 7a, 7b and 7c, respectively. Black denotes cavitated water. Note that only a third of the water tank that was simulated had been plotted here.

front arrests and inverts its motion as a closing front. Note that a closing front (this refers to the bottom edge of the cavitated region) has already formed at $t/t_i = 1.00$, 1.00 and 0.8 in Figs 8a, 8b and 8c, respectively. It is worth highlighting why the cavitated region at $t/t_i = 5.8$ appears closer to the fluid-structure interface compared to $t/t_i = 1.5$ in Fig 8a. At $t/t_i=1.0$, the entire cavitated region is in the midst of propagating towards the top of the water-tank whereupon, after reflection, it would reverse its motion towards the structure. What was shown for $t/t_i=5.8$ is the reflected cavitated region from the top boundary which is now propagating towards the structure - this is why the bottom boundary of the cavitated region appears closer to the structure at $t/t_i=5.8$ compared to, say, at $t/t_i=1.5$ in Fig 8a.

Predictions by FE and the current analytical model will now be compared for a range of incident impulses where the primary focus will be on the maximum mid-span deflection, transmitted impulse and energy. The maximum non-dimensional transmitted impulse $\bar{I}^T$,
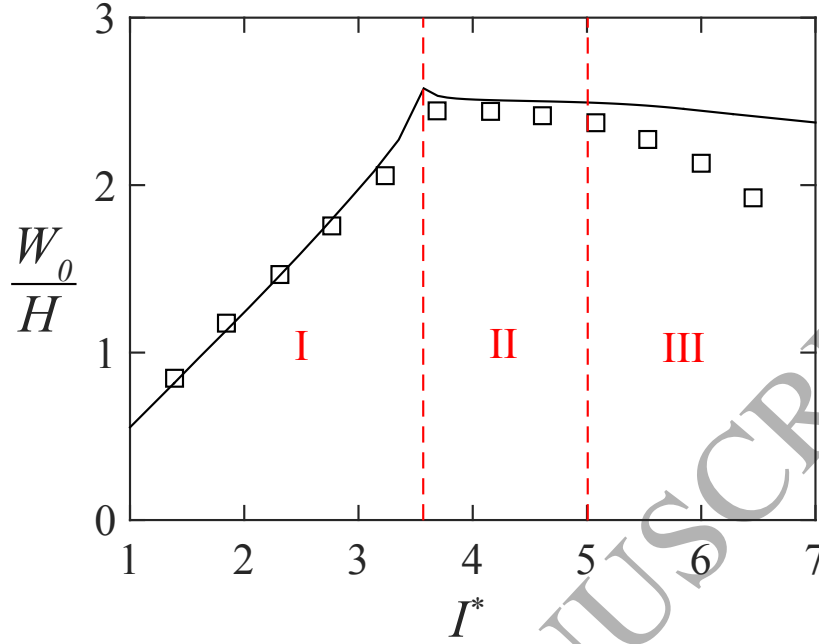
19

Figure 9: Variations of the non-dimensional mid-span deflection W_0/H with non-dimensional impulse I^* for elasto-plastic beam with $L/H = 6$ and $\beta_w = 10.9$. I, II and III indicate the three distinct damage modes predicted by the current analytical model. — current analytical model; $\square$ current FE predictions.

390 momentum $\bar{I}^K$, transmitted energy $\bar{E}^T$ and kinetic energy $\bar{E}^K$ of the elasto-plastic beam
391 are defined as follows:

$$\bar{I}^T = \max_{0 \le t < \infty}[I^T(t)/I_i], \quad \bar{I}^K = \max_{0 \le t < \infty}[I^K(t)/I_i],$$
$$\bar{E}^T = \max_{0 \le t < \infty}[E^T(t)/E_i], \quad \bar{E}^K = \max_{0 \le t < \infty}[E^K(t)/E_i]. \quad (33)$$

392 Figure 9 shows an excellent agreement for the maximum mid-span deflection W_0/H, at
393 either the point of cessation of motion or failure (if complete detachment from the supports
394 had occurred) for modes I and II. The over-prediction of $\Delta W_0/H$ in mode III with $I^*(\triangleq$
395 $2p_s t_i/H\sqrt{\sigma_Y \rho})$ is because our analytical model adopts a constant hinge length of $l = 2H$ -
396 the same assumption was also made in [17], [23] and [18] - as opposed to the approach by
397 Shen and Jones [20] where a new hinge length is re-calibrated for each data point. Both the
398 current FE and analytical models correctly predict a reduction in W_0/H with increasing I^*
399 in modes II and III - this trend is also observed in [1].

400 Figure 10 compares the non-dimensional impulse ($\bar{I}^T$ and $\bar{I}^K$) and energy ($\bar{E}^T$ and $\bar{E}^K$)
401 terms with the corresponding FE predictions. In general, the analytical predictions agree
402 well with its FE counterpart despite the under-prediction of $\bar{I}^T$ - by up to a maximum
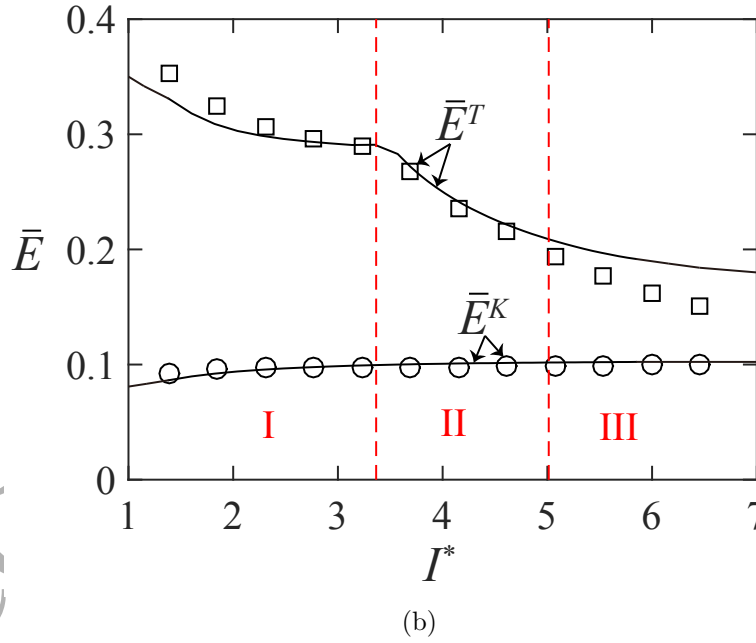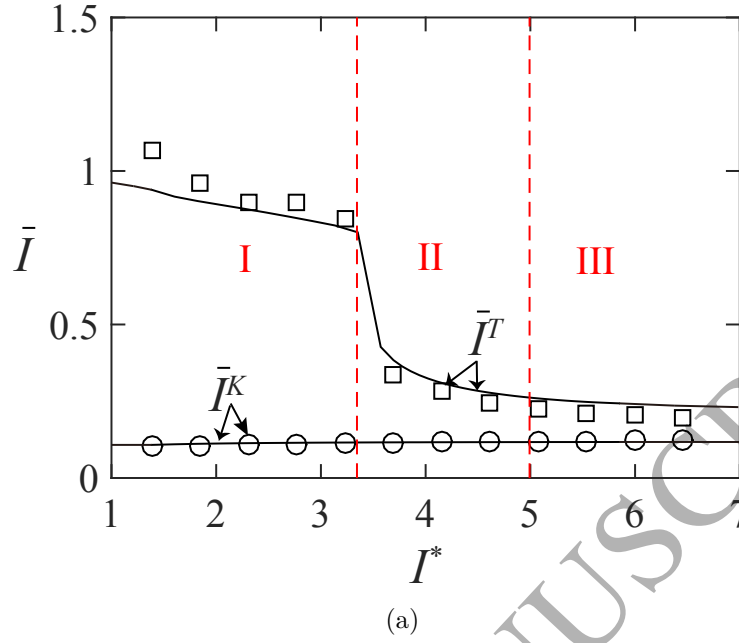
20

Figure 10: Variations of the non-dimensional maximum impulse and energy against non-dimensional impulse I^* for elasto-plastic beam with $L/H = 6$ and $\beta_w = 10.9$. I, II and III indicate the three distinct damage modes predicted by the current analytical model. — current analytical model; □ and ○ current FE predictions.

of 12.7% - in mode I. This discrepancy arises because our analytical model neglects the additional impulse transmitted by the reflection wave from the closing front.

21

In a *Type I* cavitation event (i.e. cavitation does not occur first at the fluid-structure interface), the maximum non-dimensional transmitted impulse $\bar{I}^T$ can be shown to be related to the average maximum transverse deflection, as well as the time (t_3) for complete detachment to occur; note that $t_3 = 1.66t_i$ and $t_3 = 0.8t_i$ in Figs 7b and 7c, respectively. Substituting Eqs 30 and 31 into Eq. 33, and re-arranging, gives

$$\bar{I}^T = (1/I_i) \int_0^\infty \tilde{p}_{\text{Int}}(t) \mathrm{d}t, \quad \text{if mode I} \tag{34}$$

and

$$\bar{I}^T = (1/I_i) \int_0^{t_3} \tilde{p}_{\text{Int}}(t) \mathrm{d}t, \quad \text{if mode II and III}. \tag{35}$$

Using Eqs. 15 and 24 in Eqs. 34 and 35, respectively, leads to an expression for the non-dimensional impulse $\bar{I}^T$ as follows:

$$\bar{I}^T = 2 - \frac{\rho_w c_w}{I_i} \int_0^{t_3} \int_0^L \Big[\sum_{i=1}^n \frac{\phi_i(x)\dot{w}_i(t)}{L} \Big] \mathrm{d}x\mathrm{d}t - \frac{\rho_w c_w}{I_i} \int_{t_3}^\infty \int_0^L \Big[\sum_{i=1}^n \frac{\phi_i(x)\dot{w}_i(t)}{L} \Big] \mathrm{d}x\mathrm{d}t, \quad \text{if mode I} \tag{36}$$

and

$$\bar{I}^T = 2 - 2\mathrm{e}^{-t_3/t_i} - \frac{\rho_w c_w}{I_i} \int_0^{t_3} \int_0^L \Big[\sum_{i=1}^n \frac{\phi_i(x)\dot{w}_i(t)}{L} \Big] \mathrm{d}x\mathrm{d}t, \quad \text{if mode II or III}. \tag{37}$$

Since the mid-span velocity of the beam is negligibly small during elastic rebound (see Fig 7a for example), it is reasonable to neglect the second term in Eq. 36 which simplifies to

$$\bar{I}^T = 2 - \frac{\rho_w c_w}{I_i} \int_0^{t_3} \int_0^L \Big[\sum_{i=1}^n \frac{\phi_i(x)\dot{w}_i(t)}{L} \Big] \mathrm{d}x\mathrm{d}t, \quad \text{if mode I}. \tag{38}$$

Thus, the maximum non-dimensional impulse transmitted to the beam is related to the different mechanisms through which alleviation of the transmitted impulse is achieved as follows:

$$\bar{I}^T = \bar{I}_1^T - \bar{I}_2^T - \bar{I}_3^T \tag{39}$$

where $\bar{I}_1^T = 2$ - this is a reference (or maximum) value - denotes the maximum non-dimensional impulse transmitted to a rigid beam of infinite mass; $\bar{I}_2^T = 0$ (if mode I) or $\bar{I}_2^T = 2\mathrm{e}^{-t_3/t_i}$ (if mode II or mode III) refers to the reduction of transmitted impulse as a consequence of boundary failure or detachment; and $\bar{I}_3^T = \rho_w c_w \hat{W}/I_i$ quantifies the alleviation of transmitted impulse due to both non-linear material deformation and support compliance, where $\hat{W}$ is the average transverse deflection of the beam given by

$$\hat{W} = \int_0^{t_3} \int_0^L \Big[\sum_{i=1}^n \frac{\phi_i(x)\dot{w}_i(t)}{L} \Big] \mathrm{d}x\mathrm{d}t. \tag{40}$$

Equation 39 suggests that early boundary failure (a smaller t_3 leads to higher $\bar{I}_2^T$ which is evident by comparing Fig 7c to 7b) and/or large material deformation (a higher $\bar{I}_3^T$) would

22

427 contribute to a significant reduction in the maximum non-dimensional impulse $(\bar{I}^T)$ that is
428 transmitted.

429 Figure 10a shows that $\bar{I}^T$ decreases only slightly with I^* in mode I. This is because the
430 maximum mid-span deflection W_0 - which is related to the average transverse deflection $\hat{W}$
431 - increases linearly with I^* (or I_i) in mode I (see Fig 9) which leads to a higher $\bar{I}_3^T$ and a
432 consequential reduction in $\bar{I}^T$. A sharp decrease in $\bar{I}^T$ follows the transition from mode I→II
433 because of boundary failure; a direct consequence of a jump in $\bar{I}_2^T$ from zero to a finite value
434 in Eq 39). Figure 10a shows a monotonic reduction in $\bar{I}^T$ with I^* in modes II and III. This
435 is because a higher I^* leads to premature boundary failure, resulting in a greater reduction
436 of the transmitted impulse ($\bar{I}_2^T$ in Eq. 39), see Figs 7b and 7c. It is notable that a higher I^*
437 also leads to greater transmitted impulse $\bar{I}^T$; this is a direct consequence of a lower $\bar{I}_3^T$ since
438 W_0 in modes II and III reduces monotonically with I^* as shown in Fig 9. The monotonic
439 reduction of $\bar{I}^T$ in modes II and III indicates that $\bar{I}_2^T$ could be more dominant than $\bar{I}_3^T$
440 when complete detachment occurs at the support. Figure 10 also shows that the maximum
441 transmitted energy $\bar{E}^T$ reduces monotonically with I^* in modes II and III; again, this is due
442 to pre-mature detachment of the beam from its supports. As alluded to earlier, the impulse
443 and energy transmitted 'post-detachment' are not considered. This curtails the amount of
444 impulse and energy transmitted to the elasto-plastic beams if the incident pressure pulse is
445 sufficiently intense.

446 It is interesting to note that both $\bar{I}^K$ and $\bar{E}^K$ appears relatively insensitive to I^*. This is
447 because the elasto-plastic beams, regardless of their deformation mode, always acquires the
448 maximum $\bar{I}^K$ well before the onset of cavitation in the fluid; the same was also reported in
449 [11]. The maximum $\bar{I}^K$ is already attained when the travelling plastic hinge had only just
450 started to emanate from each end of the support; hence, the central portion of the beam
451 is reminiscent of a rigid, free-standing beam. Schiffer and Tagarielli [12] also reported a
452 similar 'central rigid portion' for their fully-clamped circular composite plate in an under-
453 water blast. Recall that for rigid free-standing structures, the maximum non-dimensional
454 momentum acquired is independent of load intensity since it is only a function of FSI index
455 [2]. Because of the above, the maximum non-dimensional transmitted momentum $\bar{I}^K$ also
456 appears independent of blast impulse; similarly, for $\bar{E}^K$.

457 5. Effects of FSI on 'deformable supported' versus 'rigid free-standing' beams

458 Parametric studies will now be carried out, using the coupled fluid-beam analytical model, to
459 evaluate the sensitivity of the maximum impulse $(\bar{I}^T)$ and energy $(\bar{E}^T)$ transfer to aspect ra-
460 tio L/H and β_w ($\triangleq \rho_w c_w t_i / \rho H$ - Taylor's FSI index). Results from rigid free-standing beams
461 of an equivalent mass per unit area are also included for comparison where the maximum
462 transmitted impulse and energy - superscript F denotes free-standing - are, respectively,
463 given by [2]

$$\bar{I}^F = 2\beta_w^{-(\beta_w/\beta_w - 1)} \tag{41}$$

23

⁴⁶⁴ and

$$\bar{E}^F = 2\frac{(1 - e^{-\beta_w})^2}{\beta_w}. \tag{42}$$

⁴⁶⁵ In the parametric studies to be presented, it is worth noting the following: (1) the non-
⁴⁶⁶ dimensional maximum transmitted impulse $\bar{I}^F$ and energy $\bar{E}^F$ of rigid free-standing beams
⁴⁶⁷ are independent of peak incident pressure p_s and aspect ratio L/H but depends only on β_w;
⁴⁶⁸ (2) both the 'elasto-plastic' and 'rigid, free-standing' beams have identical mass per unit
⁴⁶⁹ area given by β_w; and, (3) cavitation always occurs at the fluid and structure interface for
⁴⁷⁰ free-standing beams at time $t_c = t_i \ln(\beta_w)/(\beta_w - 1)$ whilst it does not for the elasto-plastic
⁴⁷¹ beams (*Type I* cavitation); hence, the fluid-structure interaction time for an elasto-plastic
⁴⁷² beam is always considerably longer compared to its free-standing counterpart of the same
⁴⁷³ mass per unit area.

⁴⁷⁴ 5.1. Mode I

⁴⁷⁵ The solid blue lines in Figs 11a and 12a denote the non-dimensional maximum transmitted
⁴⁷⁶ impulse ($\bar{I}^T$ and $\bar{I}^F$) and the broken black lines denote the non-dimensional maximum
⁴⁷⁷ transmitted energy ($\bar{E}^T$ and $\bar{E}^F$). A peak incident overpressure of $p_s = 15$ MPa is used
⁴⁷⁸ throughout so that the elasto-plastic beams always deform in mode I. Figure 11a plots
⁴⁷⁹ the variation of the non-dimensional maximum impulse and energy terms as a function of
⁴⁸⁰ L/H (for a constant $\beta_w = 21.7$). For elasto-plastic beams, $\bar{I}^T$ reduces monotonically with
⁴⁸¹ L/H while $\bar{E}^T$ does not. The reason is evident by comparing two beams of different L/H,
⁴⁸² denoted by ① and ② in Fig 11b. The beam with a higher L/H, i.e. beam ②, has less average
⁴⁸³ interface pressure $\tilde{p}_{\text{Int}}/p_s$ but higher mid-span deflection W_B, leading to a smaller $\bar{I}^T$ and
⁴⁸⁴ non-monotonic decreasing $\bar{E}^T$. Figure 12a plots the maximum non-dimensional impulse and
⁴⁸⁵ energy to FSI index β_w with a constant $L/H = 10$. It shows that $\bar{I}^T$ increases monotonically
⁴⁸⁶ with increasing β_w (less mass per unit area) but $\bar{E}^T$ does not. Again, the reason is that the
⁴⁸⁷ average interface pressure $\tilde{p}_{\text{Int}}/p_s$ is higher but the mid-span deflection W_B is lower for beam
⁴⁸⁸ with a higher β_w (less mass per unit area) - compare beam ③ to ② in Fig 12b.

⁴⁸⁹ According to Eq. 39, increasing maximum mid-span deflection would lead to a greater
⁴⁹⁰ reduction of $\bar{I}^T$, i.e. by comparing the maximum mid-span deflection between beam ① and
⁴⁹¹ ② in Fig 11b or between beam ② and ③ in Fig 12b. Notice that this finding is independent
⁴⁹² of beam's geometry (i.e. two beams can have different L/H and β_w), when comparing beam
⁴⁹³ ① (in Fig 11) to ③ (in Fig 12). The above finding is potentially useful for designers as the
⁴⁹⁴ maximum mid-span deflection (in mode I) could - alone - be used as an indicator of the
⁴⁹⁵ alleviation of the impulse imparted to the structure.

⁴⁹⁶ Even though the beneficial effects of FSI, in reducing the maximum transmitted impulse for
⁴⁹⁷ a given incident pressure pulse, is clearly evident for both the deformable (and supported)
⁴⁹⁸ and rigid (and unsupported) beams, the mechanisms by which this reduction is achieved are
⁴⁹⁹ clearly different. In the former, its is due to increased elasto-plastic deformation whereas, in
⁵⁰⁰ the latter, it is due to early cavitation (a reduction in the beam's mass per unit area). We
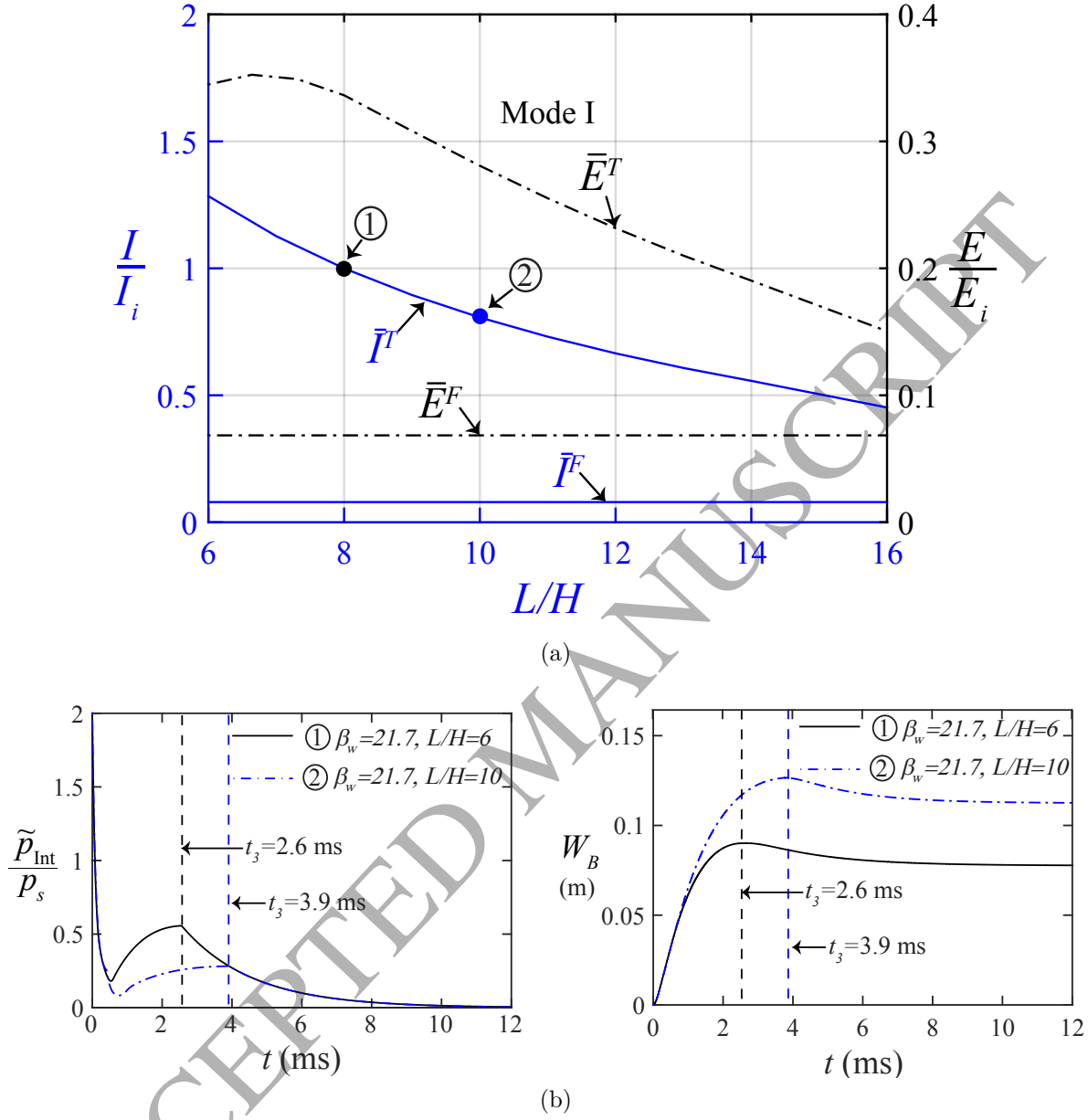⁵⁰¹ have previously shown in Eq. 39; that the maximum impulse transmitted to a deformable

24

Figure 11: (a) Analytical prediction of non-dimensional maximum impulse (— corresponds to $\bar{I}^T$ and $\bar{I}^F$) and energy (–·– corresponds to $\bar{E}^T$ and $\bar{E}^F$) for elasto-plastic beams of identical cross-section, $H = B = 0.005$ m ($\beta_w = 21.7$), deforming in mode I; and (b) Comparison of the normalised temporal average interface pressure $\tilde{p}_{\text{Int}}(t)/p_s$ and temporal mid-span deflection $W_B(t)$ for beams ① and ② in Fig 11a. Beam ① is 0.04 m (L) × 0.005 m (H) × 0.005 m (B); beam ② is 0.05 m (L) × 0.005 m (H) × 0.005m (B).

502 beam can be related to its average transverse deflection $\hat{W}$. However, unlike for rigid free-
503 standing beams where the maximum transmitted impulse scales directly to its mass per unit
504 area (or β_w) through Eq. 41, the entire temporal-history of the beam transverse velocity
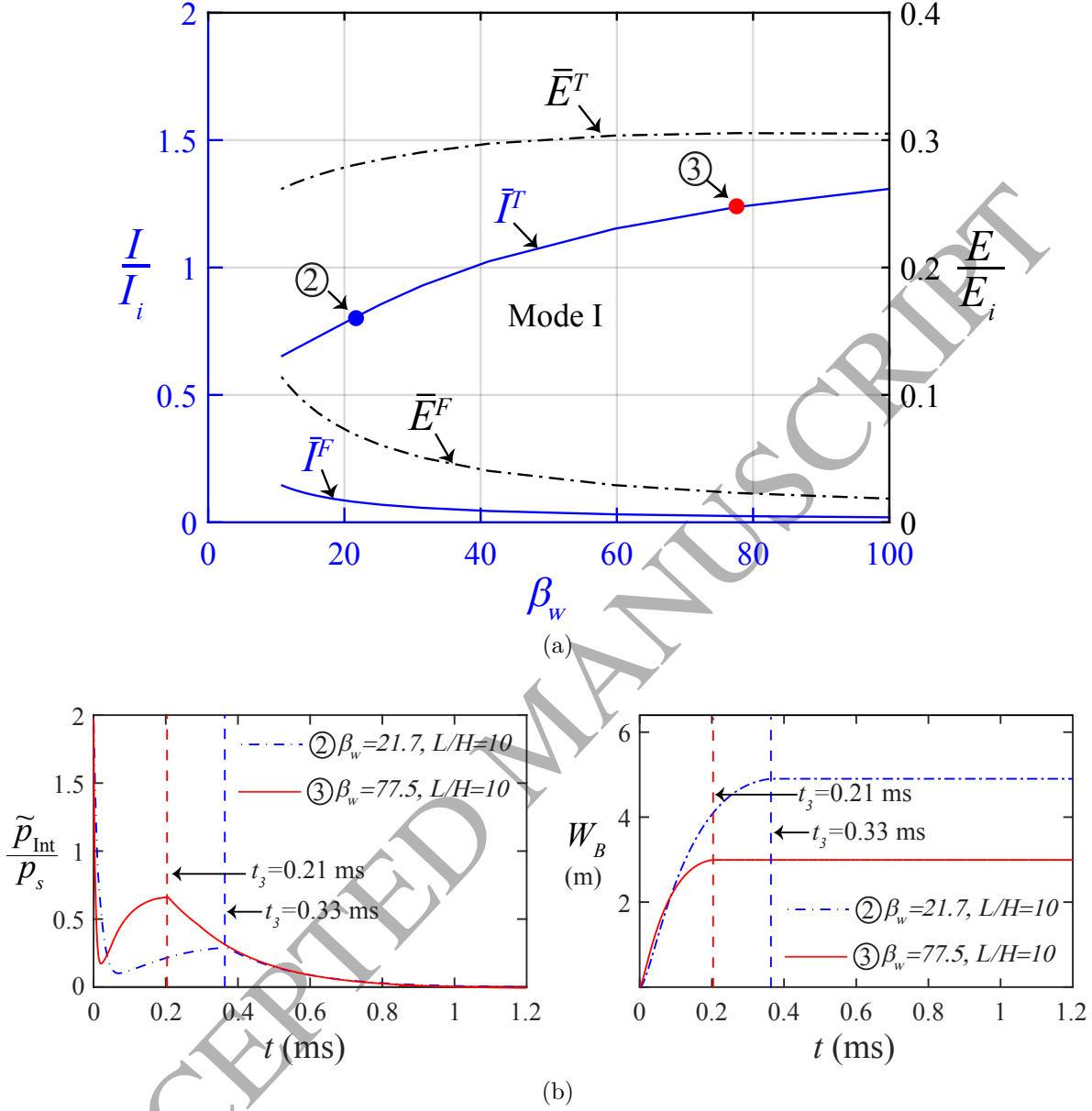505 must first be determined - this is needed to calculate $\hat{W}$ in Eq. 40 - before the maximum

25

Figure 12: (a) Analytical prediction of maximum impulse (— corresponds to $\bar{I}^T$ and $\bar{I}^F$) and energy (–·– corresponds to $\bar{E}^T$ and $\bar{E}^F$) for elasto-plastic beams with identical aspect ratio $L/H = 10$ deforming in mode I; and (b) Comparison of analytical normalised temporal average interface pressure $\tilde{p}_{\text{Int}}(t)/p_s$ and temporal mid-span deflection $W_B(t)$ for beams ② and ③ in Fig 12a. Beam ② is 0.05 m (L) × 0.005 m (H) × 0.005 m (B) ($\beta_w = 21.7$); beam ③ is 0.014 m (L) × 0.0014 m (H)× 0.0014 m (B) ($\beta_w = 77.5$).

⁵⁰⁶ transmitted impulse can be evaluated.

⁵⁰⁷ It is also worth noting that in both Figs 11a and 12a, the elasto-plastic beams have sig-
⁵⁰⁸ nificantly higher non-dimensional maximum transmitted impulse and energy compared to

26

509 free-standing beams. This is because, as alluded to earlier, the fluid-structure interaction
510 time for elasto-plastic beams are significantly longer.

5.2. Mode II

512 Variations of the maximum non-dimensional impulse and energy terms against L/H and
513 β_w for a peak incident overpressure of $p_s = 120$ MPa are shown in Figs 13 and 14 respec-
514 tively. Note that all the elasto-plastic beams shown deform in mode II. Figure 13a plots the
515 maximum non-dimensional impulse and energy terms, against the aspect ratio L/H with
516 $\beta_w = 54.3$. Both $\bar{I}^T$ and $\bar{E}^T$ do not reduce monotonically with L/H. This is because as
517 L/H increases - comparing ① to ② in Fig 13b - ① has a lower average interface pressure
518 $\tilde{p}_{\mathrm{Int}}(t)/p_s$ and, consequently, takes longer to reach its maximum mid-span deflection and for
519 complete detachment to occur. Figure 14a shows the effect of mass per unit area, or β_w,
520 on the non-dimensional impulse and energy terms for a fixed aspect ratio $L/H = 6$. It
521 shows that both $\bar{I}^T$ and $\bar{E}^T$ reduce monotonically with β_w (or less mass per unit area). As
522 opposed to Fig 13 increasing β_w - compare ② and ③ in Fig 13 - leads to a reduction in
523 the average interface pressure $\tilde{p}_{\mathrm{Int}}(t)/p_s$ and a shorter time is required to reach maximum
524 mid-span beam deflection and for complete detachment to occur.

525 Increasing L/H, as shown in Fig 13b, would lead to a lower $\bar{I}_2^T$ and a higher $\bar{I}_3^T$, while
526 increasing β_w (see Fig 14b) leads to a higher $\bar{I}_2^T$ and a lower $\bar{I}_3^T$. This explains the non-
527 monotonic decay in $\bar{I}^T$ in Fig 13a. The monotonic decay in $\bar{I}^T$ with β_w in Fig 14a suggests
528 that the effects of t_3 on the impulse transmitted in mode II could be more dominant than
529 the transverse beam deflection.

530 The beneficial effect of FSI for the rigid un-supported beam is evident in Fig 14a. However,
531 this is due to early cavitation triggered by a reduction in the beam's mass per unit area
532 as β_w increases. Furthermore, the calculation of $\bar{I}^F$ has a direct correspondence to the FSI
533 index β_w given by Eq. 41, as opposed to its deformable and supported counterparts that
534 deform in mode II.

535 The maximum non-dimensional transmitted impulse and energy are significantly smaller
536 in mode II compared to mode I for the fully-clamped elasto-plastic beams due to a loss
537 of integrity at the supports. Notwithstanding, the maximum non-dimensional transmitted
538 impulse and energy for elasto-plastic beams are still considerably greater than those of free-
539 standing beams since $\bar{I}^T > \bar{I}^F$ and $\bar{E}^T > \bar{E}^F$, as is evident in Figs 13a and 14a.

5.3. Mode III

541 Figure 15 plots the non-dimensional maximum impulse and energy for beams deforming in
542 mode III ($p_s = 160$ MPa). Note that the ratio of the plastic work absorbed through shearing
543 deformation to the total plastic work done has reached the critical ratio of $\beta_c = 0.45$ in all
544 cases. The results in Fig 15 are broadly similar to Figs 13a and 14a, despite a slight decrease
545 in $\bar{I}^T$ and $\bar{E}^T$ due to the fact that the time it takes for complete detachment to occur is shorter
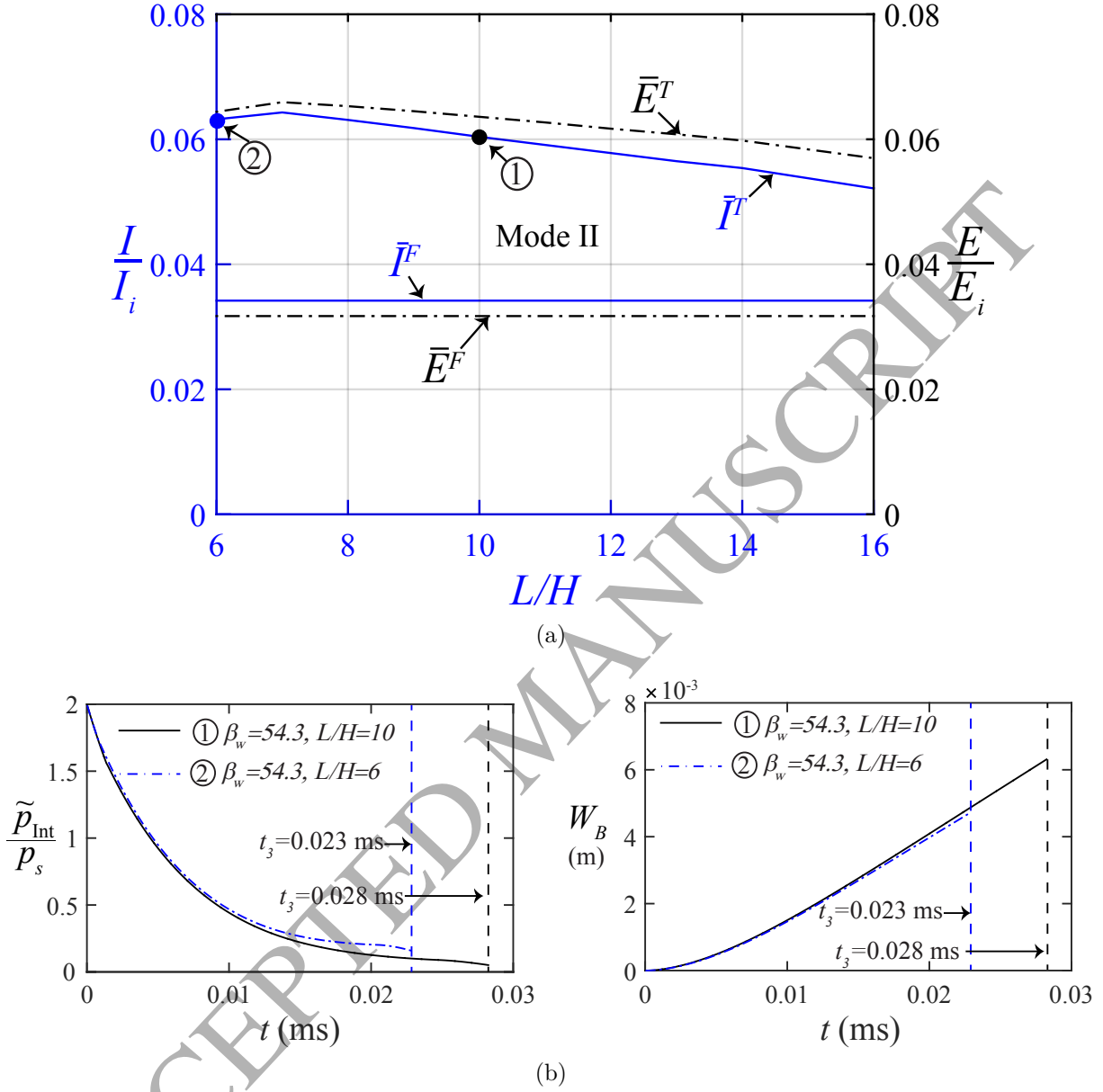
27

(a)

(b)

Figure 13: (a) Analytical prediction of non-dimensional maximum impulse (— corresponds to $\bar{I}^T$ and $\bar{I}^F$) and energy (–.– corresponds to $\bar{E}^T$ and $\bar{E}^F$) dissipation for elasto-plastic beams with identical cross-section ($H = B = 0.002$ m) deforming in mode II where $\beta_w = 54.3$; and (b) Comparison of analytical normalised temporal average interface pressure $\tilde{p}_{\text{Int}}(t)/p_s$ and temporal mid-span deflection $W_B(t)$ for beam ① and ② in Fig 13a. Beam ① has 0.02 m (L) × 0.002 m (H) × 0.002 m (B) ($\beta_w = 54.3$); beam ② has 0.012 m (L) × 0.002 m (H) × 0.002 m (B) ($\beta_w = 54.3$).

546   in mode III than in mode II - compare Figs 14a and 15b for an example. Notwithstanding,
547   the effects of L/H and β_w on maximum impulse and energy transfer in mode III are broadly
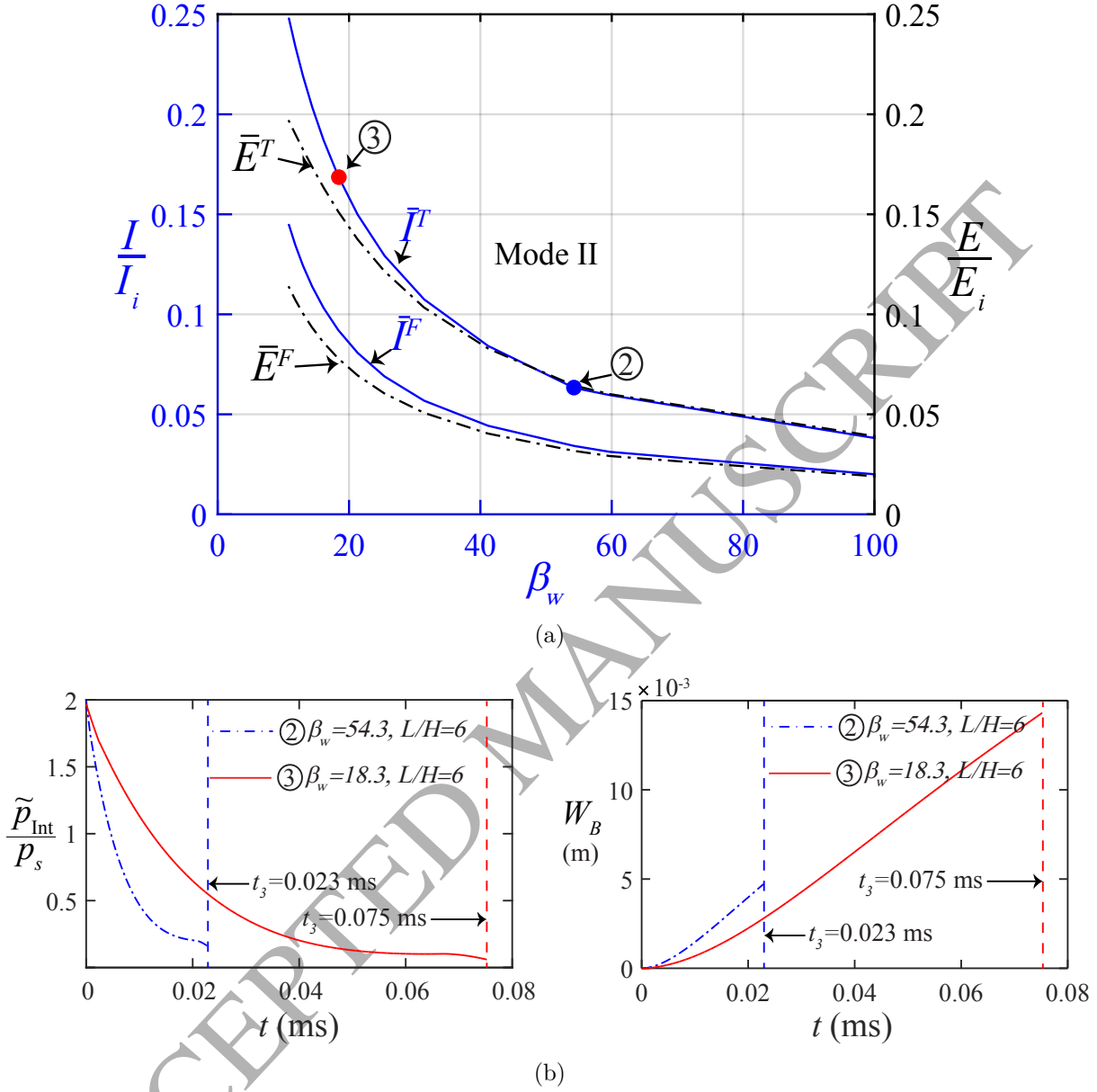548   the same as that in Figs 13a and 14a for mode II. It is evident from both figures that for

28

Figure 14: (a) Analytical prediction of non-dimensional maximum impulse (— corresponds to $\bar{I}^T$ and $\bar{I}^F$) and energy (-.– corresponds to $\bar{E}^T$ and $\bar{E}^F$) dissipation for elasto-plastic beams in mode II with the same aspect ratio $L/H = 6$; and (b) Comparison of analytical normalised temporal average interface pressure $\tilde{p}_{\text{Int}}(t)/p_s$ and temporal mid-span deflection $W_B(t)$ for beam ② and ③ in Fig 13a. Beam ② is 0.012 m (L) $\times$ 0.002 m (H) $\times$ 0.002 m (B) ($\beta_w = 54.3$); and beam ③ is 0.036 m (L) $\times$ 0.006 m (H) $\times$ 0.006 m (B) ($\beta_w = 54.3$).

549 greater impulse and energy were transmitted to the elasto-plastic beams than their free-
550 standing counterparts; this is also the case for modes I and II as shown in Figs 11a, 12a, 13a
551 and 14a. Since both $\bar{I}^T$ and $\bar{E}^T$ decrease monotonically with peak incident pressure p_s in
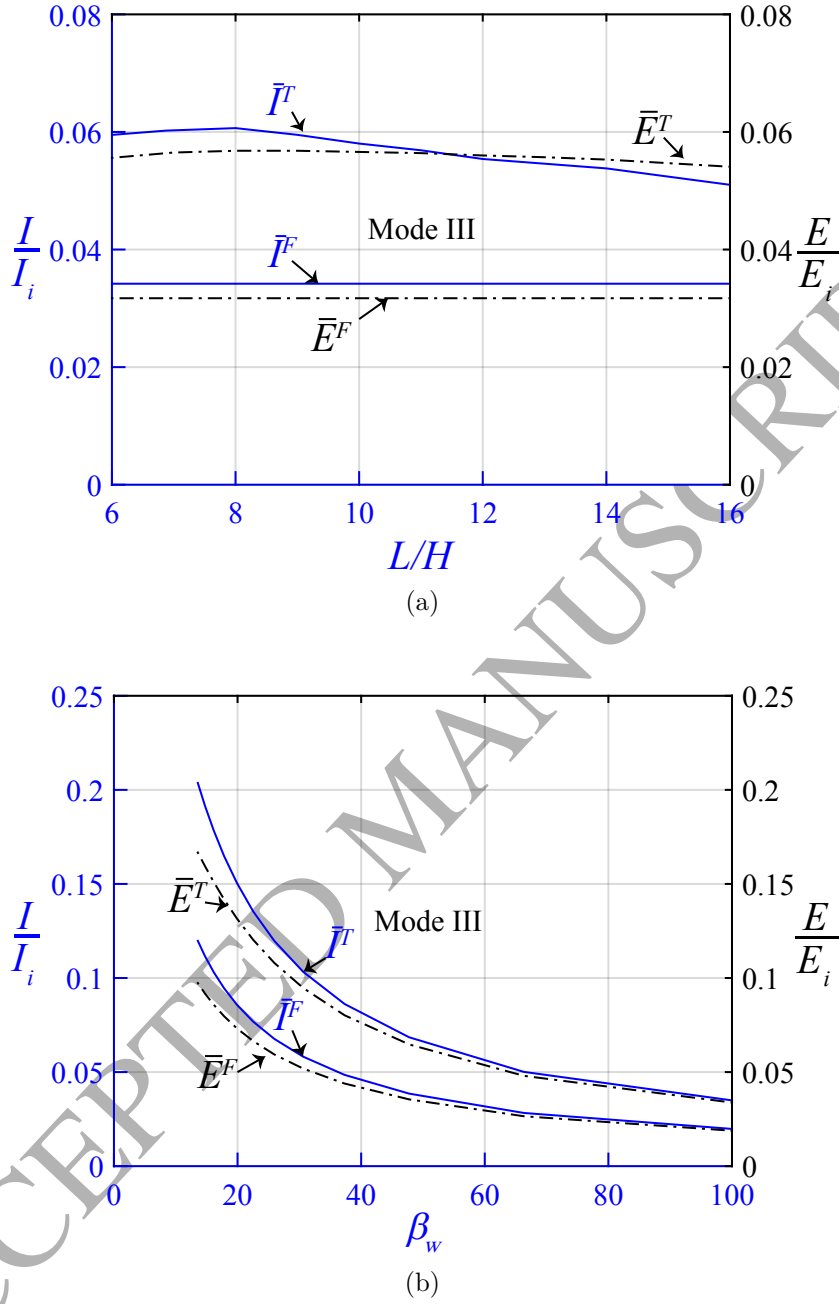
29

Figure 15: Analytical predictions of the non-dimensional maximum impulse (— corresponds to $\bar{I}^T$ and $\bar{I}^F$) and energy (-.– corresponds to $\bar{E}^T$ and $\bar{E}^F$) dissipation for two sets of elasto-plastic beams deforming in mode III: (a) of the same cross-section, $H = B = 0.002$ m ($\beta_w = 54.3$) and (b) the same aspect ratio, $L/H = 6$.

modes II and III (see Fig 10 for an example), maximum transmitted impulse and energy of elasto-plastic beams could be even less than those of rigid, free-standing beams, as a result of significant alleviation of transmitted impulse by boundary failure $\bar{I}^T_2$.

30

6. Conclusions

The dynamic response of fully-clamped elasto-plastic beam subjected to underwater blast has been investigated. An analytical model by [1] is used to predict beam deformation, interface pressure history, impulse and energy transfer in a *Type I* cavitation event where predictions were found to be in excellent agreement with 3D FE simulations. It was found that increasing non-dimensional impulse I^* leads to a reduction in the maximum mid-span deflection during modes II and III deformation. A sharp reduction in the maximum transmitted impulse accompanies the transition from mode I$\rightarrow$II and a monotonic reduction in both the maximum transmitted impulse and energy were found in modes II and III. The beneficial effect of FSI in reducing the maximum transmitted impulse to elasto-plastic beams (for a given incident pressure-pulse) was found to be dependent on two parameters: the average beam transverse deflection and the time it takes for complete detachment to occur. The latter significantly limits the impulse imparted to a structure that deforms in modes II and III but not when it is deforming in mode I. The effects of aspect ratio L/H and FSI index β_w were investigated. It was found that in mode I, an increase in aspect ratio L/H, or decrease in FSI index β_w, always leads to a reduction in the maximum impulse transmitted. In modes II and III, increasing FSI index β_w always leads to a reduction in the maximum transmitted impulse. The effects of boundary on FSI were also investigated where it was shown, as to be expected, that a significantly higher impulse and energy are transmitted to the fully clamped deformable beams, deforming in all three modes, as opposed to their free-standing counterparts of the same mass per unit area.

Appendix A - Strain energy components in the equation of motion (Eq. 25)

The dynamic response of the beam system is divided into three separate phases according to [1] and the strain energy components corresponding to each are derived below. Figure 16 presents the flow chart on the numerical implementation of the analytical model. Note that each phase of motion has its own unique set of initial conditions and associated displacement (and velocity) field. The transitional conditions between phases follow the proposal by Symonds et al. [35], which is based on the well-known 'minimum Δ_0 technique'. This technique is commonly employed to determine the starting amplitude of the 'new' velocity field by minimising the difference in kinetic energies between the velocity fields at the end of the terminating phase and at the start of the new phase [13–15].
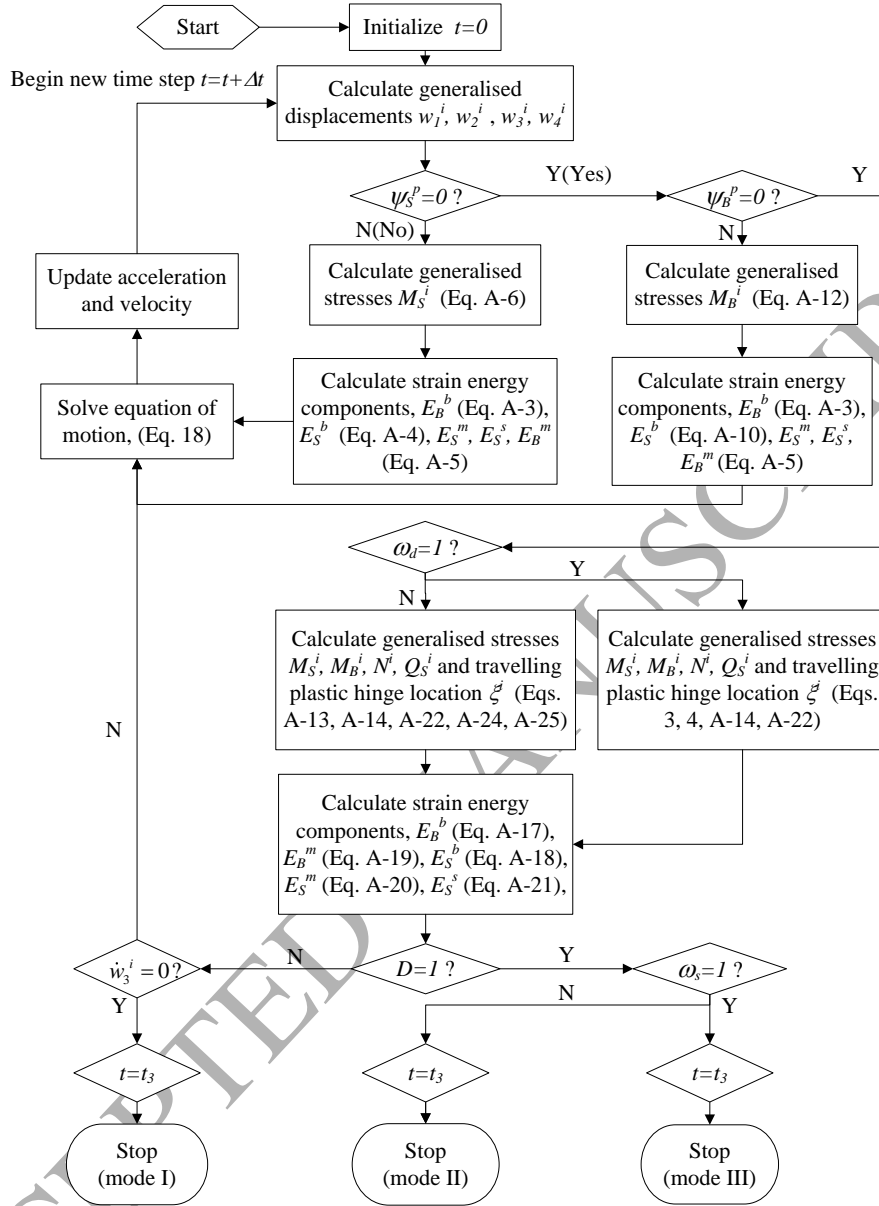
31

Figure 16: Flow-chart on the numerical implementation of the analytical model in Section 2.

Phase I: $0 < t \leq t_1$

In Phase I, it is reasonable to neglect catenary actions and transverse shear since the transverse deflection is small compared to the beam thickness, i.e. $W_B \ll H$ [13, 36]. The plastic limit function at the support is simplified according to Eq. 1

$$\psi_S^p = |\bar{M}_S| - 1. \tag{A-1}$$

Phase I motion ends when $\psi_S^p = 0$.

32

596 An admissible transverse displacement field for the right-half of the structural beam system
597 in Phase I, shown in Fig 3a, is given by [13]

$$W(x,t) = \frac{w_1(t)}{2}\left(1 + \cos\frac{\pi x}{L}\right) + w_2(t)\cos\frac{\pi x}{2L}. \tag{A-2}$$

598 The bending strain energies in the beam member and rotational spring are, respectively,

$$E_B^b(t) = \frac{EI}{2}\int_0^L \left[\frac{\partial^2 W(x,t)}{\partial x^2}\right]^2 \mathrm{d}x \tag{A-3}$$

599 and

$$E_S^b(t) = \frac{K_\phi}{2}\phi(t)^2 \tag{A-4}$$

600 where $\phi(t) = \int_0^L [\partial^2 W(x,t)/\partial x^2]\mathrm{d}x$ [13, 14]. Since $W_B \ll H$, it is reasonable to assume that
601 the strain energies due to shear and membrane are negligibly small [36]; hence,

$$E_S^s(t) = E_S^m(t) = E_B^m(t) \simeq 0. \tag{A-5}$$

602 Substituting Eqs. A-3, A-4 and A-5 into Eq. 25, and using the initial conditions $w_1 = w_2 = 0$
603 and $\dot{w}_1 = \dot{w}_2 = 0$ gives the two equations of motion for this phase. When the fully plastic
604 stress condition at the support is reached, i.e.

$$\psi_S^p = |K_\phi\phi(t)|/M_0 - 1 = 0, \tag{A-6}$$

605 it marks the end of Phase I deformation at the corresponding time of $t = t_1$.

606 *Phase II: $t_1 < t \leq t_2$*

607 In Phase II, small transverse deflection is also assumed [36–38]; hence, the influence of
608 transverse shear and catenary actions are also ignored. Therefore, the fully plastic stress
609 condition at the support - since $\psi_S^p = 0$ - reduces to

$$|\bar{M}_S| = 1 \tag{A-7}$$

610 whilst the same at the mid-span simplifies to

$$\psi_B^p = |\bar{M}_B| - 1. \tag{A-8}$$

611 Phase II motion ends when $\psi_B^p = 0$.

612 An admissible transverse displacement field for Phase II motion, shown in Fig 3b, is given
613 by [13]

$$W(x,t) = \left[w_1(t_1) + w_2(t)\right]\cos\frac{\pi x}{2L} \tag{A-9}$$

614 where $w_1(t_1)$ is the terminating amplitude of the generalised displacement from Phase I at
615 t_1. Expressions for strain energy components are identical to those previously derived for

33

Phase I (Eq. A-3 for E_B^b; Eq. A-5 for E_B^m, E_S^s and E_S^m) with the notable exception of the bending strain energy of the rotational spring at the support which is as follows:

$$E_S^b(t) = |M_S|[\phi(t) - \phi_1] = M_0[\phi(t) - \phi_1] \tag{A-10}$$

where $\phi_1 = M_0/K_\phi$. Substituting Eqs. A-3, A-5 and A-10 into Eq. 25 gives the equation of motion for Phase II. Following [35], the starting amplitude of the generalised velocity in this phase is given by

$$\dot{w}_2 = \frac{8}{3\pi}\dot{w}_1(t_1) + \dot{w}_2(t_1) \tag{A-11}$$

where $\dot{w}_1(t_1)$ and $\dot{w}_2(t_1)$ refer to the terminating amplitude of the generalised velocity from Phase I at time t_1. Once the mid-span of the beam meets the fully plastic stress condition, i.e.

$$\psi_B^p = EI\kappa(t)/M_0 - 1 = 0 \tag{A-12}$$

where $\kappa(t) = \partial^2 W(x,t)/\partial x^2|_{x=0}$ is the curvature at the mid-span, it marks the end of Phase II deformation at the corresponding time of $t = t_2$.

Phase III: $t_2 < t \le t_3$

The fully plastic stress conditions at the support and mid-span of the beam are, respectively,

$$|\bar{M}_S|(1 - \bar{Q}_S^2) + \bar{N}^2 + \bar{Q}_S^2 = 1, \quad \text{if} \quad |\bar{M}_S| > 0 \tag{A-13a}$$

$$\bar{N}^2 + \bar{Q}_S^2 = 1, \quad \text{if} \quad |\bar{M}_S| = 0 \tag{A-13b}$$

and

$$\bar{M}_B + \bar{N}^2 = 1. \tag{A-14}$$

If motion of the beam member ceases when the damage variable $D < 1$ (Mode I deformation), this will be followed by residual elastic vibration. By contrast, if this happens when $D = 1$ then the beam would fail in either mode II or mode III.

The admissible transverse displacement field at the start of Phase III motion is

$$W(x,t) = \begin{cases} w_1(t_1) + w_2(t_2) + w_3(t) & \text{if } 0 \le x \le L - \xi \\ w_4(t) + \left[w_1(t_1) + w_2(t_2) + w_3(t) - w_4(t)\right]\frac{L-x}{\xi} & \text{if } L - \xi < x < L \end{cases} \tag{A-15}$$

where $w_1(t_1)$ and $w_2(t_2)$ are terminating amplitudes of the generalised displacements from Phases I (at time t_1) and II (at time t_2), respectively. When the travelling plastic hinge reaches the mid-span, i.e. $\xi = L$, the admissible transverse displacement field becomes

$$W(x,t) = w_4(t) + \left[w_1(t_1) + w_2(t_2) + w_3(t) - w_4(t)\right]\frac{L-x}{L}. \tag{A-16}$$

34

The bending strain energies of the beam member and rotational spring are, respectively,

$$E_B^b(t) = M_B \frac{w_3(t) - w_4(t)}{\xi}, \tag{A-17}$$

and

$$E_S^b(t) = |M_S| \frac{w_3(t) - w_4(t)}{\xi}. \tag{A-18}$$

The membrane strain energies of the beam member and the horizontal axial spring may be expressed, respectively, as

$$E_B^m(t) = N\Delta_B(t) \tag{A-19}$$

and

$$E_S^m(t) = N\Delta_S(t) \tag{A-20}$$

where $\Delta_B(t) = \Delta(t)/(1+1/\sqrt{1 - Q_S^2/Q_0^2})$ is the in-plane membrane displacement at the mid-span, $\Delta(t) = [w_3(t) - w_4(t)]^2/\xi$ is the total membrane displacement and $\Delta_S(t) = \Delta(t) - \Delta_B(t)$ is the membrane displacement at the support. Here, it is assumed that in-plane membrane displacement is significant where a plastic hinge has developed. The shear strain energy of the vertical axial spring is

$$E_S^s(t) = Q_S w_4(t). \tag{A-21}$$

Note that the parameters M_S, Q_S, N, M_B, ξ and $\dot{\xi}$ in Eqs. A-17, A-19, A-18, A-20 and A-21 are unknowns. Recasting them in a non-dimensional form, viz. $\bar{M}_S$, $\bar{Q}_S$, $\bar{N}$, $\bar{M}_B$, $\bar{\xi} = \xi/L$ and $\dot{\bar{\xi}} = \dot{\xi}/L$, they will have to be computed as described below.

The non-dimensional velocity of the travelling hinge A is [20]

$$\dot{\bar{\xi}} = \frac{\sigma_Y}{\rho L^2} \frac{1.5(|\bar{M}_S| + \bar{M}_B) - 2\bar{Q}_S \dot{\bar{\xi}}(L/H)/\sqrt{3} + 6\bar{N}(\bar{w}_3 - \bar{w}_4) + \bar{\xi}[p(t)/p_c]}{\bar{\xi}(\dot{\bar{w}}_3 - \dot{\bar{w}}_4)} \tag{A-22}$$

where $\bar{w}_3 = w_3(t)/H$, $\dot{\bar{w}}_3 = \dot{w}_3(t)/H$, $\dot{\bar{w}}_4 = \dot{w}_4(t)/H$; $p_c = 4M_0/L^2$ is the fully plastic collapse force per unit length, i.e. the largest force per unit length that can be supported by the structural beam system when subjected to a pure bending moment before the bending moment at each plastic hinge reaches the fully plastic bending moment M_0 [20]. Note that when the travelling hinge A reaches the existing stationary hinge at the mid-span B, they coalesce into a single stationary hinge so that in subsequent motion

$$\dot{\bar{\xi}} = 0 \quad \text{and} \quad \bar{\xi} = 1. \tag{A-23}$$

The calculations of $\bar{M}_S$, $\bar{Q}_S$, $\bar{N}$, $\bar{M}_B$ would depend on whether damage had initiated. If the state variable $\omega_d < 1$, then $\bar{M}_S$, $\bar{Q}_S$ and $\bar{N}$ are governed by normality requirements so that plastic flow must occur at a non-negative energy dissipation rate since they have met the

fully plastic stress condition (Eq. A-13). Therefore, according to [20],

$$\bar{N}\left(1 + \frac{1}{\sqrt{1 - \bar{Q}_S^2}}\right) = 2(\bar{w}_3 - \bar{w}_4) \tag{A-24a}$$

$$\bar{Q}_S\left[\frac{2}{\sqrt{1 - \bar{Q}_S^2}} - \frac{|\bar{M}_S|}{\sqrt{1 - \bar{Q}_S^2}}\right] = \frac{4\bar{\xi}(L/H)\dot{\bar{w}}_4}{\sqrt{3}(\dot{\bar{w}}_3 - \dot{\bar{w}}_4)} \tag{A-24b}$$

if $|\bar{M}_S| > 0$, and

$$\bar{N}\left[\frac{2\dot{\bar{w}}_4}{\sqrt{3}\bar{Q}_S} + \frac{\dot{\bar{w}}_3 - \dot{\bar{w}}_4}{\bar{\xi}(L/H)}\right] = 2\frac{(\bar{w}_3 - \bar{w}_4)(\dot{\bar{w}}_3 - \dot{\bar{w}}_4)}{\bar{\xi}(L/H)} \tag{A-25}$$

if $|\bar{M}_S| = 0$. If the state variable $\omega_d = 1$, then the non-dimensional bending moment $\bar{M}_S$, membrane force $\bar{N}$ and shear force $\bar{Q}_S$ are governed by Eq. 3. Note that the non-dimensional bending moment $\bar{M}_B$ remains governed by fully plastic stress condition established for the mid-span ($\psi_B^p = 0$) in Eq. A-14.

To calculate $\bar{M}_S$, $\bar{Q}_S$, $\bar{N}$ and $\bar{M}_B$, they have to be expressed as functions of $\bar{w}_3$, $\bar{w}_4$, $\dot{\bar{w}}_3$, $\dot{\bar{w}}_4$, $\bar{\xi}$, $\dot{\bar{\xi}}$ and t through Eqs. A-13, A-14, A-22, A-24 and A-25 if $\omega_d < 1$; and through Eqs. 4, 3, A-14 and A-22 if $\omega_d = 1$. The temporal evolution of these parameters are obtained by solving the aforementioned equations using the well-known 4th order Runge-Kutta method with the initial conditions of $w_3 = w_4 = 0$ and $\dot{w}_4 = 0$. The starting amplitude of the generalised velocity $\dot{w}_3$ for Phase III is given by

$$\dot{w}_3 = \frac{12}{\pi^2}\dot{w}_2(t_2) \tag{A-26}$$

where $\dot{w}_2(t_2)$ refers to the terminating amplitude of the generalised velocity from Phase II at time t_2. Phase III deformation ends at time t_3 if motion of the beam member ceases i.e.

$$\dot{w}_3(t_3) = 0. \tag{A-27}$$

If the damage variable $D < 1$ when this occurs, then the beam fails in mode I. Otherwise, a mode II or mode III failure would ensue if $D = 1$.

References

[1] Y. Yuan, P. Tan, K. Shojaei, P. Wrobel, Large deformation, damage evolution and failure of ductile structures to pulse-pressure loading, Int. J. Solids Struct. 96 (2016) 320 – 339. doi:10.1016/j.ijsolstr.2016.05.019.
URL http://www.sciencedirect.com/science/article/pii/S0020768316301068

[2] G. I. Taylor, The Pressure and Impulse of Submarine Explosion Waves on Plates. In *The Scientific Papers of Sir Geoffrey Ingram Taylor*, Cambridge: Cambridge University Press, 1941.

[3] G. J. McShane, V. S. Deshpande, N. A. Fleck, The underwater blast resistance of metallic sandwich beams with prismatic lattice cores, J. Appl. Mech. 74 (2) (2006) 352–364. doi:10.1115/1.2198549.
URL http://dx.doi.org/10.1115/1.2198549

[4] G. J. McShane, V. S. Deshpande, N. A. Fleck, Underwater blast response of free-standing sandwich plates with metallic lattice cores, Int. J. Impact Eng. 37 (11) (2010) 1138 – 1149. doi:10.1016/j.ijimpeng.2010.05.004.
URL http://www.sciencedirect.com/science/article/pii/S0734743X10000941

[5] Z. Xue, J. W. Hutchinson, A comparative study of impulse-resistant metal sandwich plates, Int. J. Impact Eng. 30 (10) (2004) 1283 – 1305. doi:10.1016/j.ijimpeng.2003.08.007.
URL http://www.sciencedirect.com/science/article/pii/S0734743X03001039

[6] V. S. Deshpande, N. A. Fleck, One-dimensional response of sandwich plates to underwater shock loading, J. Mech. Phys. Solids 53 (11) (2005) 2347 – 2383. doi:10.1016/j.jmps.2005.06.006.
URL http://www.sciencedirect.com/science/article/pii/S0022509605001213

[7] N. A. Fleck, V. S. Deshpande, The resistance of clamped sandwich beams to shock loading, J. Appl. Mech. 71 (3) (2004) 386–401. doi:10.1115/1.1629109.
URL 10.1115/1.1629109

[8] M. T. Tilbrook, V. S. Deshpande, N. A. Fleck, Underwater blast loading of sandwich beams: Regimes of behaviour, Int. J. Solids Struct. 46 (17) (2009) 3209 – 3221. doi:10.1016/j.ijsolstr.2009.04.012.
URL http://www.sciencedirect.com/science/article/pii/S0020768309001747

[9] L. F. Mori, D. T. Queheillalt, H. N. G. Wadley, H. D. Espinosa, Deformation and failure modes of i-core sandwich structures subjected to underwater impulsive loads, Exp. Mech. 49 (2) (2009) 257–275. doi:10.1007/s11340-008-9166-9.
URL http://dx.doi.org/10.1007/s11340-008-9166-9

[10] E. H. Kennard, Cavitation in an elastic liquid, Phys. Rev. 63 (1943) 172–181. doi:10.1103/PhysRev.63.172.
URL http://link.aps.org/doi/10.1103/PhysRev.63.172

[11] A. Schiffer, V. L. Tagarielli, N. Petrinic, A. C. F. Cocks, The response of rigid plates to deep water blast: Analytical models and finite element predictions, J. Appl. Mech. 79 (6) (2012) 061014–061014. doi:10.1115/1.4006458.
URL http://dx.doi.org/10.1115/1.4006458

[12] A. Schiffer, V. L. Tagarielli, The response of circular composite plates to underwater blast: Experiments and modelling, J. Fluids Struct. 52 (2015) 130 – 144. doi:10.1016/j.jfluidstructs.2014.10.009.
URL http://www.sciencedirect.com/science/article/pii/S0889974614002242

[13] G. K. Schleyer, S. S. Hsu, A modelling scheme for predicting the response of elastic-plastic structures to pulse pressure loading, Int. J. Impact Eng. 24 (8) (2000) 759 – 777. doi:10.1016/S0734-743X(00)00019-1.
URL http://www.sciencedirect.com/science/article/pii/S0734743X00000191

[14] G. Langdon, G. Schleyer, Inelastic deformation and failure of profiled stainless steel blast wall panels. part ii: analytical modelling considerations, Int. J. Impact Eng. 31 (4) (2005) 371 – 399. doi:10.1016/j.ijimpeng.2003.12.011.
URL http://www.sciencedirect.com/science/article/pii/S0734743X03002367

[15] W. J. Stronge, T. X. Yu, Dynamic Models for Structural Plasticity, Springer, 1993.

[16] ABAQUS, *User's Manual Version 6.10*, Dassault Systemes Simulia Corp., Providence, RI. (2010).

[17] H. M. Wen, Deformation and tearing of clamped work-hardening beams subjected to impulsive loading, Int. J. Impact Eng. 18 (4) (1996) 425 – 433. doi:10.1016/0734-743X(95)00053-D.
URL http://www.sciencedirect.com/science/article/pii/0734743X9500053D

[18] M. Alves, N. Jones, Impact failure of beams using damage mechanics: Part i: analytical model, Int. J. Impact Eng. 27 (8) (2002) 837 – 861. doi:10.1016/S0734-743X(02)00017-9.
URL http://www.sciencedirect.com/science/article/pii/S0734743X02000179

[19] S. B. Menkes, H. J. Opat, Broken beams, Exp. Mech. 13 (11) (1973) 480–486. doi:10.1007/BF02322734.
URL http://dx.doi.org/10.1007/BF02322734

[20] W. Q. Shen, N. Jones, A failure criterion for beams under impulsive loading, Int. J. Impact Eng. 12 (1) (1992) 101 – 121. doi:10.1016/0734-743X(92)90359-2.

37

731 URL http://www.sciencedirect.com/science/article/pii/0734743X92903592
732 [21] N. Jones, Structural Impact, Cambridge: Cambridge University Press, 1989.
733 [22] T. X. Yu, F. L. Chen, A further study of plastic shear failure of impulsively loaded clamped beams,
734   Int. J. Impact Eng. 24 (6-7) (2000) 613 – 629. doi:10.1016/S0734-743X(99)00038-X.
735   URL http://www.sciencedirect.com/science/article/pii/S0734743X9900038X
736 [23] N. Jones, Plastic failure of ductile beams loaded dynamically, J. Eng. Industry 98 (1) (1976) 131–136.
737   doi:10.1115/1.3438805.
738   URL http://dx.doi.org/10.1115/1.3438805
739 [24] T. Nonaka, Some interaction effects in a problem of plastic beam dynamics, J. Appl. Mech. 34 (1967)
740   623–43.
741 [25] G. N. Nurick, G. C. Shave, The deformation and tearing of thin square plates subjected to impulsive
742   loads: an experimental study, Int. J. Impact Eng. 18 (1) (1996) 99 – 116. doi:10.1016/0734-743X(95)
743   00018-2.
744   URL http://www.sciencedirect.com/science/article/pii/0734743X95000182
745 [26] N. Jones, A theoretical study of the dynamic plastic behavior of beams and plates with finite-deflections,
746   Int. J. Solids Struct. 7 (8) (1971) 1007 – 1029. doi:10.1016/0020-7683(71)90078-3.
747   URL http://www.sciencedirect.com/science/article/pii/0020768371900783
748 [27] G. S. Langdon, A. Ozinsky, S. C. K. Yuen, The response of partially confined right circular stainless
749   steel cylinders to internal air-blast loading, Int. J. Impact Eng. 73 (2014) 1 – 14. doi:10.1016/j.
750   ijimpeng.2014.05.002.
751   URL http://www.sciencedirect.com/science/article/pii/S0734743X14001092
752 [28] J. H. Williams, Fundamentals of applied dynamic, New York: John Wiley & Sons, 1996.
753 [29] J. W. Hancock, A. C. Mackenzie, On the mechanisms of ductile failure in high-strength steels subjected
754   to multi-axial stress-states, J. Mech. Phys. Solids 24 (2) (1976) 147 – 160. doi:10.1016/0022-5096(76)
755   90024-7.
756   URL http://www.sciencedirect.com/science/article/pii/0022509676900247
757 [30] G. R. Johnson, W. H. Cook, A constitutive model and data for metals subjected to large strains,
758   high strain rates and high temperatures, in: Proceedings of 7th International Symposium on Ballistics,
759   Netherlands, pp. 541, 1983.
760 [31] A. Shojaei, G. Z. Voyiadjis, P. Tan, Viscoplastic constitutive theory for brittle to ductile damage in
761   polycrystalline materials under dynamic loading, Int. J. Plast. 48 (2013) 125 – 151. doi:10.1016/j.
762   ijplas.2013.02.009.
763   URL http://www.sciencedirect.com/science/article/pii/S0749641913000466
764 [32] Y. Liang, A. V. Spuskanyuk, S. E. Flores, D. R. Hayhurst, J. W. Hutchinson, R. M. McMeeking, A. G.
765   Evans, The response of metallic sandwich panels to water blast, J. Appl. Mech. 74 (1) (2005) 81–99.
766   doi:10.1115/1.2178837.
767   URL http://dx.doi.org/10.1115/1.2178837
768 [33] Y. Yuan, P. J. Tan, Deformation and failure of rectangular plates subjected to impulsive loadings, Int.
769   J. Impact Eng. 59 (2013) 46 – 59. doi:10.1016/j.ijimpeng.2013.03.009.
770   URL http://www.sciencedirect.com/science/article/pii/S0734743X13000730
771 [34] M. M. Swisdak, Explosion effects and properties - Part II: explosion effects in water. In Technical
772   report, Naval Surface Weapons Center, DahlgrEn VA, Cambridge: Cambridge University Press, 1978.
773 [35] P. S. Symonds, H. Kolsky, J. M. Mosquera, Simple elastic-plastic method for pulse loading - comparisons
774   with experiments and finite element solutions, Inst. Phys. Conf. Ser. 70 (1984) 479–486.
775 [36] B. Izzuddin, A simplified model for axially restrained beams subject to extreme loading, Int. J. Steel
776   Struct. 5 (2005) 421–429.
777 [37] A. S. Fallah, L. Louca, Pressure-impulse diagrams for elastic-plastic-hardening and softening single-
778   degree-of-freedom models subjected to blast loading, Int. J. Impact Eng. 34 (4) (2007) 823 – 842.
779   doi:10.1016/j.ijimpeng.2006.01.007.
780   URL http://www.sciencedirect.com/science/article/pii/S0734743X06000212
781 [38] A. S. Fallah, E. Nwankwo, L. A. Louca, Pressure-impulse diagrams for blast loaded continuous beams

38

782   based on dimensional analysis, J. Appl. Mech. 80 (5) (2013) 051011–051011. doi:10.1115/1.4023639.
783   URL http://dx.doi.org/10.1115/1.4023639